OpenFOAM® Journal

Volume 6 [Full Papers], Pages 99–124
ISSN: 2753-8168

Implementation and Validation of a Three-Phase Phase-Change Solver with Merging Theory for Gas–Liquid Cavitating Flows

Mehrdad Kazemi[1,*] and Nikolai Kornev[1]

[1]Faculty of Mechanical Engineering and Marine Technologies, Chair of Modeling and Simulation, Albert-Einstein-Str.2, 18059 Rostock, Germany
Email address: mehrdadkazemi70@gmail.com

Email address: nikolai.kornev@uni-rostock.de

DOI: https://doi.org/10.51560/ofj.v6.169
Results with version(s): OpenFOAM® v2406
Repository: https://github.com/Mehrdad-1991/inter3PhasemergingChangeFoam.git

Abstract. Numerical prediction of ventilated cavitation remains challenging due to the coexistence of liquid, vapor, and non-condensable gas and the strong unsteadiness of the resulting flow. This paper presents the implementation and validation of a three-phase VOF cavitation solver in `OpenFOAM` for water, vapor, and air flows, in which phase change is modeled only between liquid and vapor while the non-condensable gas is transported as an additional immiscible phase. To represent air-vapor co-existence effects inside cavitating structures, the solver incorporates a merging-theory-based effective pressure closure within a stabilized pressure and velocity coupling framework, together with bounded volume-fraction transport and mixture-density regularization to enhance robustness for strongly unsteady regimes.

The solver is validated against published experimental measurements for a Clark Y hydrofoil with and without air injection. The results demonstrate that the implementation reproduces the reported mean pressure-distribution trends and captures consistent changes in unsteady pressure-fluctuation characteristics induced by ventilation. Overall, the proposed open-source implementation provides a numerically robust platform for simulating three-phase ventilated cavitation in configurations relevant to engineering applications.

1. Introduction

Cavitation is characterized by the nucleation, growth, and collapse of vapor structures in a liquid when the local static pressure falls below the saturation vapor pressure. In hydraulic systems such as fuel injectors, turbines, marine propellers, hydrofoils, and underwater vehicles, cavitation is frequently associated with performance degradation, vibration, noise emission, and material erosion [1–6]. These adverse effects motivate continued efforts to understand cavitation dynamics and to develop effective mitigation strategies.

Cavitation control approaches are commonly classified as passive or active. Passive methods rely on geometric or surface modifications to alter the near-wall flow and cavitation inception characteristics, whereas active methods introduce external actuation, often via injection of a non-condensable gas (typically air) [7–9]. Air injection can modify the cavity topology and unsteady behaviour, and it has been reported to reduce cavitation-induced noise and vibration under appropriate operating conditions [10–13]. However, the outcome depends strongly on the injection configuration and operating point. The injection location, injection rate, and the cavitation number influence whether air injection stabilizes the cavity dynamics or introduces additional unsteadiness [14–16]. For example, Hilo et al. reported that air injection near the leading edge of a NACA0012 hydrofoil reduced cavity extent and suppressed noise for moderate cavitation numbers [10]. Malekshah et al. showed that moving the injection position closer to the cavitation inception region on a Clark Y hydrofoil reduced the shedding frequency and vibration levels [11]. At the same time, several studies indicate that overly large injection rates may increase pressure fluctuations or acoustic signatures, implying the existence of an operating-dependent optimum [14–16].

* Corresponding author

Received: 1 September 2025 , Accepted: 19 June 2026, Published: 15 September 2026

The flow physics of ventilated and partially ventilated cavities is further complicated by unsteady ventilation and gas entrainment mechanisms. Hao et al. demonstrated experimentally that sinusoidal modulation of the air injection rate can generate smaller but more dynamically unstable cavities than steady ventilation, highlighting the role of boundary-layer development and entrainment processes [16]. Mao et al. reported that controlled air injection can mitigate pressure pulsations and vibration in hydraulic pumps, but that performance deteriorates when the injection rate exceeds an optimal threshold [12]. Yoon et al. distinguished internal flow features of ventilated partial cavities, including intermittently fluctuating open cavities and more stable two-branch cavities, emphasizing that cavity stability is sensitive to the ventilation regime [13]. Recent three-dimensional experiments by Hilo et al. further showed that even low air injection rates can increase cavity coverage and decrease shedding frequency, and that moderate air injection can reduce high-frequency sound pressure levels above approximately 2 kHz, albeit with reported changes in drag and low-frequency acoustic content [17].

Reliable numerical prediction of air-injected cavitating flows, therefore, requires models that (i) represent the three-phase system (liquid, vapor, and non-condensable gas), (ii) include phase change between liquid and vapor, and (iii) remain numerically robust under strongly unsteady conditions. In this context, the present work focuses on developing a three-phase VOF-based phase-change solver within OpenFOAM [18]. The implementation builds on the general modelling line of Schnerr-Sauer type cavitation closures [19] as used and extended in subsequent works [20, 21]. In addition, a merging-theory-based pressure closure is incorporated to represent the influence of non-condensable gas on the pressure field entering the phase-change closure, consistent with the modelling direction reported in the cavitation literature [22–24].

As a practical starting point, the solver framework of Dueholm et al. [21] was adopted, which is based on an Euler-Euler formulation with a VOF interface-capturing strategy for three immiscible phases. In the present study, the solver development proceeds in two stages. First, numerically stabilizing modifications are introduced to enable stable simulations for cavitating hydrofoils with active air injection, which was not achieved with the baseline implementation for the target configuration. Second, the merging approach, which is similar to that used by Malekshah et al. [15], is adapted into a form compatible with a VOF volume fraction field α and implemented consistently within the phase-change closure. The resulting solver is denoted `inter3PhasemergingChangeFoam`.

This work is part of a broader research effort aimed at reducing the acoustic signature of cavitating propellers through air injection. To address this practically important problem, it was necessary to develop a specialized CFD tool. Similar work was conducted in [15] using a merging theory implemented in Ansys. Our objective was to implement this theory in OpenFOAM, followed by verification and validation of the implementation. In doing so, we have created a tool capable of solving our specific problem while also making it accessible to a wider user community. To keep the manuscript self-contained, the governing equations solved by the solver and the final closure relations are stated explicitly in the main text, while detailed derivations are provided in Appendix A. The primary contribution is the solver implementation (including compatibility with the targeted OpenFOAM release and both static and dynamic mesh operation), together with a VOF-consistent merging activation criterion and a numerically robust treatment of pressure and mixture density for air-injection cavitating flows.

2. Theoretical Background

The theoretical foundation of the present solver, which accounts for three-phase cavitating flows using a Volume of Fluid (VOF) formulation, is based on the OpenFOAM solver `interPhaseChangeFoam`. This solver provides a one-field formulation for incompressible multiphase flows with phase change and serves as the baseline for the developments introduced in this work.

In the present formulation, three volume-fraction fields are considered. Indices 1, 2, and 3 denote the liquid phase, the vapor phase of the liquid, and the non-condensable gas phase, respectively. Accordingly, α_1, α_2, and α_3 represent the volume fractions of liquid, vapor, and non-condensable gas, and satisfy the constraint

$$\alpha_1 + \alpha_2 + \alpha_3 = 1, \tag{1}$$

which enforces that each computational cell is fully occupied by the three phases. A single velocity field $\mathbf{U}$ is solved for the mixture, following the standard one-field approach adopted in the `interFoam` family of solvers. All phases are assumed incompressible and isothermal, meaning that the density of each individual phase remains constant in time. Turbulence effects are modelled using the Reynolds-averaged Navier-Stokes (RANS) framework with the k-ω SST turbulence model [25]. Unsteady simulations are performed to capture the transient nature of flow.

The next step involved modifying the `alphaEqn` and cavitation model source files, such as `SchnerrSauer.C` and `SchnerrSauer.H`. To maintain compatibility with the original two-phase cavitation formulation while extending it to a third phase, the modified version was renamed to `SchnerrSauer3`. This adaptation was introduced by Dueholm et al. [21].

The governing equations and the derivation of the three-phase formulation adopted here are summarized in Appendix A.

In a three-phase VOF formulation, the mixture density is defined as a volume-fraction-weighted sum of the individual phase's densities,

$$\rho = \alpha_1\rho_1 + \alpha_2\rho_2 + \alpha_3\rho_3, \tag{2}$$

where ρ_1, ρ_2, and ρ_3 denote the constant densities of the liquid, vapor, and non-condensable gas phases, respectively.

The conservation of mass for the mixture is therefore written as

$$\frac{\partial\rho}{\partial t} + \nabla\cdot(\rho\mathbf{U}) = 0, \tag{3}$$

which accounts for local changes in mixture density caused by phase transport and phase change.

The corresponding mixture momentum equation, expressed in conservative form, reads

$$\frac{\partial(\rho\mathbf{U})}{\partial t} + \nabla\cdot(\rho\mathbf{U}\otimes\mathbf{U}) = -\nabla p + \nabla\cdot\boldsymbol{\tau}_{\text{eff}} + \rho\mathbf{g} + \mathbf{f}_\sigma, \tag{4}$$

where p is the pressure, $\boldsymbol{\tau}_{\text{eff}}$ is the effective viscous and turbulent stress tensor, $\mathbf{g}$ denotes the gravitational acceleration, and $\mathbf{f}_\sigma$ represents the surface-tension forces.

In Eqns. (3) and (4), the density ρ appears explicitly despite the incompressible assumption for each phase. This is because incompressibility implies constant density for each individual phase, but not a constant mixture density. As the volume fractions α_i evolve due to advection and phase change, the local mixture density varies accordingly, requiring a variable-density formulation.

The first term in Eqn. (3) represents the local temporal change of mixture density, while the second term accounts for the convective transport of mass by the mixture velocity. Eqn. (4) describes the conservation of linear momentum of the mixture. The transient term $\partial(\rho\mathbf{U})/\partial t$ represents the temporal variation of momentum, and the convective term $\nabla\cdot(\rho\mathbf{U}\otimes\mathbf{U})$ accounts for momentum transport by advection. The pressure-gradient term $-\nabla p$ drives the flow, while the stress-divergence term $\nabla\cdot\boldsymbol{\tau}_{\text{eff}}$ includes both molecular viscosity and turbulence-model contributions. The term $\rho\mathbf{g}$ accounts for gravity, and $\mathbf{f}_\sigma$ represents capillary forces arising from surface tension at phase interfaces, treated using a continuum surface-force approach.

In the present work, several theoretical closures and modelling assumptions (e.g. boundedness of volume fractions, mixture-density regularization, and merging-theory activation criteria) do not admit a compact representation purely in continuous analytical form, but are instead naturally defined through their discrete realization within the VOF framework. For this reason, selected code-level expressions are presented alongside their mathematical formulation. These expressions should be understood not as low-level implementation details, but as the explicit algorithmic definition of the governing closures required to reproduce the model. This approach is consistent with established practice in the OpenFOAM literature and ensures full transparency and reproducibility of the theoretical formulation.

As previously mentioned, the present development incorporates several physics-based stabilization techniques into the solver `inter3PhaseChangeFoam` from [21]. A key stabilization measure is the bounding of volume fractions α_{liquid} and $\alpha_{\text{non-condensable gas}}$. Due to numerical or model-related inaccuracies, volume fractions may occasionally fall outside the physical range $[0, 1]$. To mitigate this issue, the liquid volume fraction is constrained as shown in Lst. 1.

```
1 volScalarField limitedAlpha1(min(max(alpha1_, scalar(0)), scalar(1)));
```

Listing 1. Bounding of the liquid volume fraction.

This approach is also used in the original `interPhaseChangeFoam` solver [18]. A similar limitation is applied to the volume fraction of the non-condensable gas phase, as shown in Lst. 2.

```
1 volScalarField limitedAlpha3(min(max(alpha3_, scalar(0)), scalar(1)));
```

Listing 2. Bounding of the non-condensable gas volume fraction.

In both `interPhaseChangeFoam` and `inter3PhaseChangeFoam`, the transport equations are used to compute non-evaporating phase fractions. Assuming that the sum of the volume fractions equals unity,

the vapor fraction can be expressed using Eqn. (1). From a physical perspective, the sum of the volume fractions of the liquid and the non-condensable gas must also remain bounded between 0 and 1. Accordingly, we define the bounded sum in Lst. 3.

```
volScalarField limitedAlpha13(min(max(alpha1_ + alpha3_, scalar(0)), scalar(1)));
```

Listing 3. Bounding of the combined liquid and non-condensable gas volume fraction.

Alternatively, using the already limited values, the same bounded sum can be written as shown in Lst. 4.

```
volScalarField limitedAlpha13(min(max(limitedAlpha1 + limitedAlpha3, 0)), 1));
```

Listing 4. Alternative bounded form using already limited volume fractions.

This ensures that the volume fraction of the vapor phase also remains within the physically valid interval $[0, 1]$.

An additional stabilization strategy concerns the computation of the mixture density. Given the distinct densities of the three phases and their respective volume fractions, the mixture density can be calculated as shown in Lst. 5.

```
volScalarField rho
(
    limitedAlpha1*rho1() + limitedAlpha2*rho2() + limitedAlpha3*rho3()
);
```

Listing 5. Volume-fraction-weighted mixture-density calculation.

However, Dueholm et al. [21] noted that the model does not account for diffusion between the gas phases, which limits its applicability in cases where such interaction is significant. One observed issue was solver divergence associated with nonphysical mixture properties arising from unbounded or inconsistent intermediate volume-fraction fields. To address this, the mixture density is constrained to remain above the lowest density among fluids, namely vapor density, as shown in Lst. 6.

```
volScalarField rho
(
    max(limitedAlpha1*rho1() + limitedAlpha2*rho2() + limitedAlpha3*rho3(), rho2())
);
```

Listing 6. Lower-bounded mixture-density calculation.

This density lower bound helps stabilize simulations at higher Courant numbers.

The merging-theory-based pressure closure is summarized as follows. In the original cell-volume-based interpretation, the merging condition is evaluated from the local amounts of liquid, vapor, and non-condensable gas inside a computational cell. Since the volume fraction is defined as the ratio of phase volume to cell volume, i.e. $\alpha_i = V_i/V_{\text{cell}}$, the same criterion can be expressed directly in terms of volume fractions.

Let α_i^* denote the bounded value of the corresponding volume fraction. In the present implementation, merging is activated in cells where the liquid volume fraction falls below $\alpha_{\ell,\text{crit}} = 0.99$, corresponding to a combined vapor and non-condensable gas content above approximately 1%, and where the vapor fraction is not smaller than the non-condensable gas fraction. The activation coefficient is defined as

$$M = \min\left[H\left(0.99 - \alpha_1^*\right), H\left(\alpha_2^* - \alpha_3^*\right)\right], \tag{5}$$

where $H(\cdot)$ is the Heaviside step function, corresponding to the OpenFOAM `pos` operator. Thus, $M = 1$ when both activation conditions are satisfied and $M = 0$ otherwise. Equivalently, the implemented activation criterion is satisfied when $\alpha_1^* \leq 0.99$ and $\alpha_2^* \geq \alpha_3^*$. The corresponding OpenFOAM implementation of the activation coefficient is shown in Lst. 7.

```
volScalarField cond1 = pos(scalar(0.99) - limitedAlpha1);
volScalarField cond2 = pos(limitedAlpha2 - limitedAlpha3);
volScalarField mergeC = min(cond1, cond2);
```

Listing 7. Implementation of the merging-activation coefficient.

The merged pressure is then evaluated by first defining the excess pressure above saturation and the local gas–vapor volume-fraction ratio as

$$p_{g2} = \max(p - p_v, 0), \qquad r = \max\left(\frac{\alpha_3^*}{\alpha_2^* + \varepsilon}, \varepsilon\right), \tag{6}$$

where ε is a small numerical constant used to avoid division by zero. The pressure associated with the merged gas–vapor structure is computed as

$$p_{m,\text{merged}} = p_v + p_{g2} r^{\gamma}, \tag{7}$$

where γ is the polytropic exponent. The effective pressure entering the cavitation model is finally obtained as

$$p_m = M p_{m,\text{merged}} + (1 - M) p_v. \tag{8}$$

Therefore, when the merging criterion is inactive, the classical saturation pressure p_v is recovered. When merging is active, p_v is replaced by the effective pressure p_m, which accounts for the contribution of the non-condensable gas within vapor-containing structures. The corresponding OpenFOAM implementation is given in Lst. 8.

```
volScalarField pg2 = max(p - pv, dimensionedScalar("zero", p.dimensions(), 0.0));
volScalarField ratio = max(limitedAlpha3 / (limitedAlpha2 + SMALL), scalar(SMALL));
volScalarField pmMerged = pv + pg2 * Foam::pow(ratio, gamma);
volScalarField pm = mergeC*pmMerged + (scalar(1) - mergeC)*pv;
```

Listing 8. Implementation of the effective merged pressure used by the cavitation model.

Here, p denotes the local pressure, p_v is the vapor saturation pressure, γ is the polytropic exponent, and `SMALL` is used to avoid division by zero. The variables `pg2`, `ratio`, `pmMerged`, and `pm` correspond to p_{g2}, r, $p_{m,\text{merged}}$, and p_m, respectively.

In other words, in this approach, the saturation pressure p_v used in the classical cavitation model is replaced by an effective merged pressure p_m, which accounts for the presence of non-condensable gas inside the vapor structures. Since $p_m \geq p_v$, the driving pressure difference $(p - p_m)$ is reduced compared to $(p - p_v)$, leading to a suppression of evaporation and condensation rates whenever merging is active.

Physically, this represents the smoothing effect of non-condensable gas within cavitating structures, which limits the intensity of bubble collapse.

To enhance the robustness of the solver, the pressure equation (p_{rgh}) has been modified relative to the formulation presented by Dueholm et al. [21]. Specifically, all terms have been rearranged to the left-hand side (LHS) of the equation. This restructuring increases the diagonal dominance of the resulting matrix system, which in turn improves the numerical stability of the pressure solution. The resulting pressure-equation form is shown in Lst. 9.

```
    fvScalarMatrix p_rghEqn
    (
          fvc::div(phiHbyA)
        - fvm::laplacian(rAUf, p_rgh)
        - (vDotvP - vDotcP)(mixture->pSat() - rho*gh)
        + fvm::Sp(vDotvP - vDotcP, p_rgh)
    );
```

Listing 9. Rearranged pressure-equation matrix used to improve numerical stability.

Although the present investigation focuses exclusively on simulations using a fixed mesh, additional developments have been carried out to extend the solver's applicability to dynamic mesh configurations—more precisely, those involving the Arbitrary Mesh Interface (AMI). While the solver described by Dueholm et al. [21] includes most of the required components for handling mesh motion, attempts to simulate such cases resulted in the runtime error shown in Lst. 10.

```
tmp<N4Foam14GeometricFieldIdNS_12fvPatchFieldENS_7volMeshEEE> deallocated
```

Listing 10. Runtime deallocation error encountered during dynamic-mesh simulations.

To address this issue, two key internal fields were refactored: `rAUf`, the face-interpolated inverse of the diagonal momentum matrix (originally a temporary `volScalarField`), and `Uf`, the face-centered velocity field (of type `surfaceVectorField`). These variables were converted from under-the-hood temporaries into explicitly declared fields, making them persistent and accessible during the simulation. This modification successfully resolved the *deallocation* error, enabling robust execution of simulations involving mesh motion.

The resulting solver, which is capable of handling dynamic mesh motion via the AMI, is also publicly available on GitHub under the name `inter3PhasemergingChangeDyMFoam`. This naming convention aligns with the standard solver structure in OpenFOAM to maintain consistency with the official framework.

In the previous solver implementation, simulations with Courant numbers exceeding unity frequently resulted in numerical divergence. By contrast, the current solver has been successfully applied to cases with Courant numbers exceeding 50 without exhibiting instability. This substantial increase in the allowable Courant number is advantageous, as it enables the use of larger time steps. Unless high temporal resolution is required due to specific physical phenomena or accuracy constraints, increasing the time step in this manner is beneficial, as it accelerates convergence and reduces overall computational cost.

3. **Numerical setup**

This investigation utilizes a Clark Y hydrofoil with both the chord and span measuring 0.07 meters. The hydrofoil is analyzed at an angle of attack of 8 degrees. To ensure alignment with the computational and experimental setup by [15], current study numerical model adopts the same geometric and domain configurations. The inlet boundary is positioned 3.2 times the chord length ahead of the hydrofoil's leading edge, while the outlet lies 5.8 chord lengths behind the trailing edge. The vertical size of the domain between two horizontal planes is 2.5 chords.

Ventilation and pressure measurements are conducted through small 0.5 mm diameter holes located at taps 1 to 11.

On the suction side of the hydrofoil, eleven taps (numbered 1–11) are positioned in a row at varying streamwise distances from the leading edge, as detailed in Tab. 9. They are used both for ventilation and pressure measurements. For visual clarity, Fig. 1 highlights only Tap 1 and Tap 5, while the full set of tap locations is provided in Tab. 9.

A steady inlet velocity of 10.45 m/s is applied at the domain's entrance, and a pressure outlet condition is used at the exit to control cavitation within the flow field. No-slip conditions are enforced on the hydrofoil surface and both horizontal walls, while the lateral boundaries are treated as symmetry [15].

Air is supplied through either the first hole—referred to as Tap 1, injections—to analyze the impact of injection position. The air flow rates considered are 0, and 1 liter per minute.

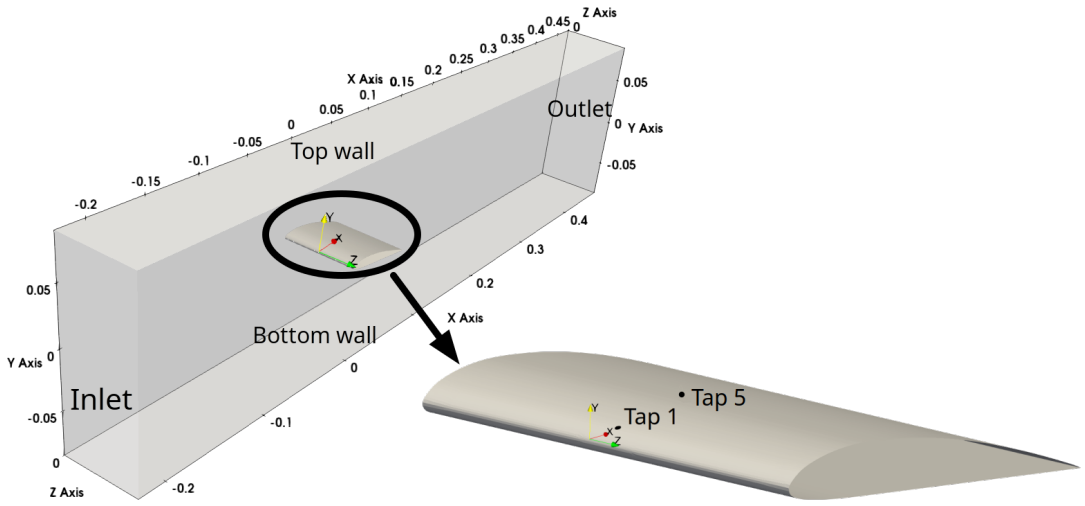

Figure 1. Computational domain

Simulations were performed using the URANS framework in OpenFOAM, incorporating core solver functionalities by Jasak [26] and Weller et al. [18]. The developed solver `[inter3PhasemergingChangeFoam]` was used for all computations.

The convective terms were treated using the `filteredLinear` scheme, which combines central differencing with a limited upwind term, constrained to a maximum of 20% based on local-to-face gradient ratios. Pressure gradients were computed using the linear Green–Gauss method. The Crank–Nicolson scheme was employed for time discretization.

Due to the inherently unsteady flow, residuals displayed semi-periodic oscillations. Average residuals were approximately 10^{-5} for velocity, 10^{-5} for pressure, 10^{-6} for ω, 10^{-5} for k, and 10^{-6} for α. The cumulative continuity error remained below 10^{-6}, with stepwise errors typically under 10^{-7}.

Tables 1 and 2 summarize the computational domain, boundary conditions, and operating parameters used in the simulations. The cavitation number is defined as

$$\sigma = \frac{p_{\text{inlet}} - p_v}{\frac{1}{2}\rho U_{\text{inlet}}^2}, \tag{9}$$

where p_v is the saturation vapor pressure, ρ is the liquid density, and p_{inlet} and U_{inlet} denote the inlet pressure and velocity.

Table 1. Summary of geometry, domain dimensions, and operating conditions.

Parameter	Value
Hydrofoil profile	Clark Y
Chord c [m]	0.07
Span s [m]	0.07
Angle of attack α [°]	8
Inlet distance upstream [c]	3.2
Outlet distance downstream [c]	5.8
Top boundary height [c]	2.5
Inlet velocity U_∞ [m/s]	10.45

Table 2. Boundary conditions used in the simulations.

Boundary	**U**	p or p_{rgh}	Volume fractions $(\alpha_1, \alpha_2, \alpha_3)$
Inlet	fixedValue $(U_\infty, 0, 0)$	zeroGradient	$\alpha_1 = 1, \alpha_2 = 0, \alpha_3 = 0$
Outlet	zeroGradient	fixedValue (p_{out})	zeroGradient
Hydrofoil	noSlip	zeroGradient	zeroGradient
Top/Bottom walls	noSlip	zeroGradient	zeroGradient
Side boundaries	symmetryPlane	symmetryPlane	symmetryPlane
Injector (Tap1)	flowRateInletVelocity	$p = p_{\text{inlet}}$	α_3 inlet (air)

4. **Results**

4.1. **Validation and Verification**

Experimental and numerical data obtained by Malekshah et al. [15] for the pressure coefficient distribution over a Clark Y hydrofoil with a chord length of 0.07 m at cavitation number $\sigma = 1.1$, are used for validation purposes for both air injection and non-injection scenarios. For the sake of brevity, experimental setup and sensor configuration are not described in this manuscript, and the reader is referred to Malekshah et al. [15] for full experimental details. Additionally to experimental data, CFD results of [15] include the lift and drag coefficients, which are used as benchmarks for validation in the present study. The pressure, lift, and drag coefficients were calculated using the following relations:

$$C_p = \frac{p_{\text{local}} - p_\infty}{\frac{1}{2}\rho U_{\text{inlet}}^2} \tag{10}$$

$$C_l = \frac{L}{\frac{1}{2}\rho U_{\text{inlet}}^2 A} \tag{11}$$

$$C_d = \frac{D}{\frac{1}{2}\rho U_{\text{inlet}}^2 A} \tag{12}$$

Here, p_∞ is the ambient pressure, ρ is the fluid density, U_{inlet} is the inlet velocity, and A is the reference surface area.

As a preliminary step, simulations of cavitating flow without air injection were conducted to assess the solver's capability in capturing cavitation phenomena. This also served to verify that the integration of the merging theory does not influence the results when the third phase (i.e., non-condensable gas) is absent.

To this end, a grid independence study and a time-averaging sensitivity analysis were conducted. Based on the results of these investigations, the optimal grid resolution and averaging interval were selected. With these settings in place, the lift coefficient (C_l), drag coefficient (C_d), and pressure coefficient (C_p) were compared against the reference data from Malekshah et al. [15].

The next phase of the study applies the same validation and verification procedure to cases involving air injection, in order to evaluate the solver's performance in modeling three-phase cavitating flow, which includes the presence of a non-condensable gas and the application of the merging model.

4.2. **Baseline Verification and Validation: Two-Fluid System (Without Air Injection)**

The grid independence study based on the time-averaged lift coefficient ($\overline{C_l}$) and time-averaged drag coefficient ($\overline{C_d}$) is summarized in Tab. 3. Additionally, the distribution of the time-averaged pressure coefficient (C_p) along the hydrofoil surface—sampled at the mid-span line—is illustrated in Fig. 3, providing further insight into mesh sensitivity. As shown in both Fig. 3 and Tab. 3, the mesh with approximately 1.020 million cells exhibits grid-converged behavior. This mesh is therefore adopted for all subsequent simulations.

A time-averaging independence study was also carried out using $\overline{C_d}$ and $\overline{C_l}$. The results, shown in Fig. 2, reveal that averaging over approximately 0.3014 seconds—equivalent to 45 flow-through times—yields a quasi-steady solution with minimal temporal variation. This averaging interval is used throughout the remainder of the study.

Table 3. Grid independence study based on ($\overline{C_l}$) and ($\overline{C_d}$).

Grid Size [Millions]	($\overline{C_d}$)	Rel. Change [%]	($\overline{C_l}$)	Rel. Change [%]
0.310	0.11509		0.80411	
0.498	0.11470	-0.33	0.81627	1.51
1.020	0.11506	0.31	0.81203	-0.52
1.838	0.11580	0.64	0.81423	0.27
3.686	0.11428	-1.31	0.81401	-0.03

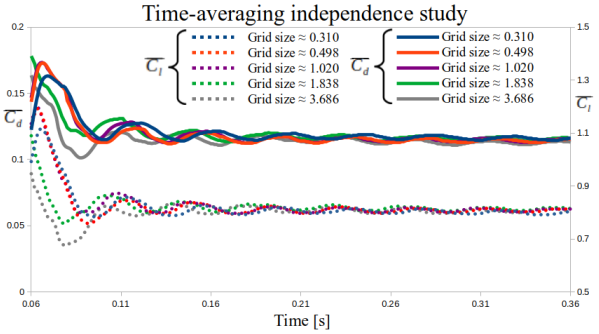

Figure 2. Time-averaging independence study based on $\overline{C_l}$ and $\overline{C_d}$.

As further justification for selecting a grid size of approximately 1.020 million cells, the distribution of the time-averaged pressure coefficient ($\overline{C_p}$) along the hydrofoil surface is shown in Fig. 3. This figure also includes a comparison between the current numerical results and both the experimental and numerical data from Malekshah et al. [15]. It is evident that the results of the present study exhibit a smaller discrepancy relative to the experimental data, in comparison to the numerical predictions of Malekshah et al. [15].

The mesh consisting of approximately 1.020 million cells yields a local non-dimensional wall distance (y^+) on the hydrofoil surface with an average value of `2.94E+01` and a maximum value of `6.31E+01`. Accordingly, standard wall functions were employed for near-wall treatment throughout this investigation.

Figure 3 presents the $\overline{C_p}$ extracted along a mid-span line and compared with the data from Malekshah et al. [15] for the cavitation number $\sigma = 1.1$. The comparison confirms excellent agreement between the present study and the experimental data, while a minor deviation is observed relative to their numerical results.

In Fig. 3, differences between the medium and fine grids are small, indicating that the solution is close to grid-independent; the full set of grid levels is nevertheless reported to document the verification procedure and demonstrate robustness with respect to mesh refinement.

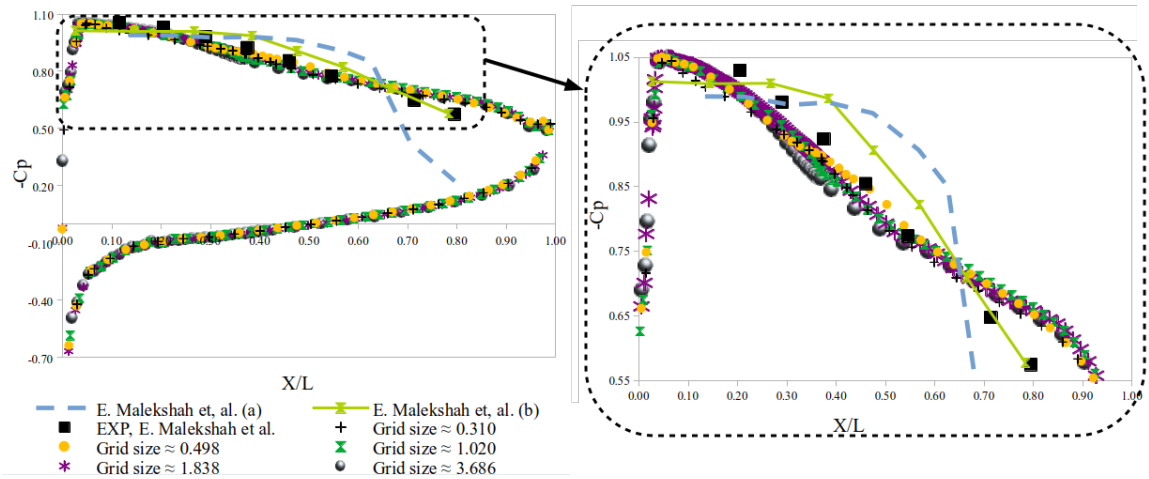

Figure 3. Grid independence and validation study of the $\overline{C_p}$ along the hydrofoil surface at mid-span. Comparison is shown against the experimental and numerical results from Malekshah et al. [15]. Grid size is indicated in millions of cells.

A comparison of the time-averaged drag ($\overline{C_d}$) and lift ($\overline{C_l}$) coefficients from the present study with the computational results reported by Malekshah et al. [15] was also conducted. For mesh sizes of 0.310, 0.498, 1.020, 1.838, and 3.686 million cells, the deviations in $\overline{C_d}$ were found to be 3.25%, 2.56%, 2.80%, 3.08%, and 0.38%, respectively. In contrast, the deviations in $\overline{C_l}$ were comparatively larger, at 13.00%, 14.09%, 14.07%, 14.34%, and 13.14%, respectively.

Both $\overline{C_d}$ and $\overline{C_l}$ exhibit oscillatory convergence behavior. Therefore, the grid uncertainty (U_G) was estimated using the approach for oscillatory convergence, as proposed by Stern et al. [27]. The associated uncertainty is calculated using:

$$U_G = \frac{1}{2}(S_U - S_L) \tag{13}$$

where S_G is the simulation result obtained on the finest grid, S_U represents the upper bound of the oscillating solution across grid refinements, and S_L denotes the corresponding lower bound. This formulation provides an estimate of the numerical uncertainty due to mesh resolution in cases of non-monotonic (oscillatory) convergence.

The uncertainty associated with grid refinement and relative grid uncertainty, defined as U_G and U_G/S_G, was computed for both $\overline{C_d}$ and $\overline{C_l}$ using the three finest mesh levels. The resulting uncertainties were 1.620×10^{-3} and 1.433% for $\overline{C_d}$, and 4.769×10^{-3} and 0.593% for $\overline{C_l}$, respectively.

Table 4. Parameters of monotonic convergence for $\overline{C_p}$ at taps 2 and 7, using the three finest grids.

	R_G	GR	P_G	C_G	δ^*_{RE}	U_G/S_G	δ^*_G/S_G	U_{G_C}/S_G	U_v	E
Tap 2	2.9178	1.2610	-4.6170	-1.1136	-2.099E-03	0.657%	0.227%	0.430%	2.721E-02	2.218E-02
Tap 7	0.1187	1.2610	9.1890	12.5810	2.444E-03	3.665%	3.982%	3.665%	3.428E-02	3.226E-02

Where R_G is the convergence ratio; GR is the grid refinement ratio; P_G is the estimated order of accuracy based on Richardson extrapolation; C_G is the correction factor accounting for higher-order terms; δ^*_{RE} is the estimated discretization error on the finest grid; U_G/S_G is the uncorrected relative grid uncertainty; δ^*_G/S_G is the relative estimated error; U_{G_C}/S_G is the corrected uncertainty after applying C_G; U_v is the total validation uncertainty including numerical and experimental sources; and E is the comparison error between simulation and experimental measurements.

Table 4 presents the verification results for the time-averaged pressure coefficient $\overline{C_p}$, following the monotonic convergence framework introduced by Stern et al. [27] and implemented using the methodology outlined by Kazemi et al. [28]. The analysis was conducted at two representative pressure tap locations—Tap 2 and Tap 7—located along the mid-span of the hydrofoil surface.

For validation, the numerical predictions of $\overline{C_p}$ at these tap positions were compared with the experimental data reported by Malekshah et al. [15]. The relative deviations from the experimental values are 3.6% at Tap 2 and 0.4% at Tap 7, respectively.

It should be emphasized that U_d, representing the uncertainty in the experimental data, is not explicitly defined in the reference study by Malekshah et al. [15]. Therefore, a conservative estimate of 2.5% of the experimental value was assumed for validation purposes in this work.

Following the guideline established by Stern et al. [27], if the absolute value of the comparison error $|E|$ is less than the total validation uncertainty U_v, it implies that the combined numerical and experimental errors are within the estimated bounds, and thus, validation is achieved. This condition is satisfied in the present study, thereby supporting the reliability of the simulation results.

Despite the inherent complexity of the flow field and the non-negligible deviation from experimental data, the present results exhibit improved agreement with the experimental measurements compared to the CFD predictions reported by Malekshah et al. [15].

As an additional check of mesh sensitivity for an *unsteady* metric, the pressure signal $p(t)$ at selected taps was analyzed in the frequency domain. Following the procedure described by Heo and Kim [29], the dominant cavitation shedding frequency f_{shed} can be estimated by applying a Fourier transform to $p(t)$ and identifying the strongest peak in the low-frequency band. The corresponding spectral amplitude $A_{p'}(f_{\text{shed}})$ was then extracted and compared across mesh resolutions.

Table 5. Grid-independence study without air injection based on the pressure-fluctuation spectral amplitude at the primary shedding frequency f_{shed}, evaluated at Tap 10 and Tap 2.

Grid size [million cells]	$A_{p'}(f_{\text{shed}})$ at Tap 10	$A_{p'}(f_{\text{shed}})$ at Tap 2
0.30	0.1197	0.0281
0.49	0.1262	0.0224
1.00	0.1293	0.0231
1.80	0.1272	0.0242
3.50	0.1275	0.0243

Based on Tab. 5, grid independence for the unsteady metric $A_{p'}(f_{\text{shed}})$ can be regarded as effectively achieved with the mesh containing approximately 1.0×10^6 cells. At Tap 10, the amplitude changes from 0.12937 (1.0M) to 0.12730 (1.8M) and 0.12759 (3.5M), corresponding to variations of approximately -1.6% and -1.4% relative to the 1.0M value. At Tap 2, the amplitudes are 0.02314 (1.0M), 0.02421 (1.8M), and 0.02433 (3.5M), i.e., increases of approximately $+4.6\%$ and $+5.1\%$ relative to the 1.0M value. Importantly, the difference between the two finest meshes is small at both locations (about 0.2% at Tap 10 and 0.5% at Tap 2), indicating diminishing sensitivity to further refinement beyond 1.0M cells. Therefore, the 1.0M mesh provides a practical compromise between computational cost and accuracy for capturing the shedding-frequency pressure-fluctuation amplitude in the present configuration.

4.3. **Extended Verification and Validation: Three-Fluid System (With Air Injection)**

The results presented thus far demonstrate that the developed solver `inter3PhasemergingChangeFoam` performs with high accuracy, and that the implementation of the merging theory does not affect the solution in scenarios where the third fluid (i.e., non-condensable gas) is absent. This preliminary validation was a necessary step to ensure the reliability of the solver prior to its application in the intended use case involving three-fluid cavitating flows.

Having established this foundation, the study now proceeds to the second stage: evaluating the solver under conditions where the third fluid is present and active. In this phase, the influence of air injection and the interaction of the non-condensable gas with the liquid and vapor phases are examined.

All results presented in this section, as well as those in the remainder of the results chapter, correspond to simulations conducted at a cavitation number of $\sigma = 1.1$, with an air injection rate of $Q = 1\,\text{L/min}$ introduced through Tap 1. The pressure boundary condition at the injector is set to the ambient pressure p_∞, and the velocity boundary condition is derived from the specified volumetric flow rate using the inlet velocity.

As in the previous section, a similar verification and validation procedure is applied to evaluate the solver's performance in a more complex three-fluid flow configuration. However, several important differences must be highlighted.

First, the time-averaged lift and drag coefficients ($\overline{C_l}$ and $\overline{C_d}$) are not reported in [15], which is the only source available for validation in cases involving air injection for this geometry. Second, in the study by Malekshah et al. [15], the pressure coefficient C_p provided for air injection scenarios appears to be

based on instantaneous pressure data rather than time-averaged results (see Nomenclature and Eqn. 32 in [15]).

While validation typically relies on time-averaged data, the significant unsteadiness in the simulated pressure coefficient C_p makes the examination of instantaneous values more informative. Our results presented below lead us to believe that the air injection results reported in [15] may not represent true time-averaged values, but instead reflect specific instants dominated by the flow's inherent unsteadiness.

A detailed analysis of the current simulation data confirms strong unsteadiness in C_p when air is injected. Figure 4 illustrates these fluctuations, which are likely caused by the presence of the third fluid—non-condensable gas—introducing additional instability into the flow. This leads to large variations in instantaneous pressure throughout the simulation.

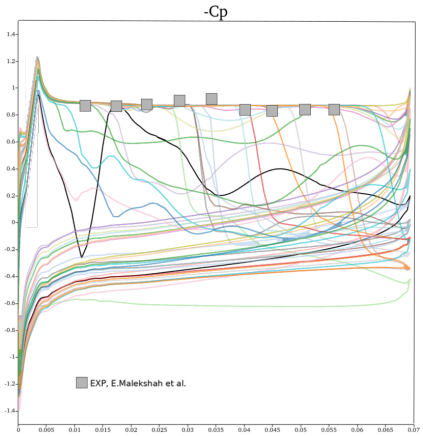

Figure 4. Temporal variation of the pressure coefficient C_p at the mid-span of the hydrofoil for the case with air injection. (Different colors denote C_p profiles sampled at different time steps)

Further analysis revealed that extracting the pressure coefficient C_p at the time instant corresponding to the maximum cavitation volume produces distributions that closely align with those reported in [15]. Accordingly, for comparative purposes in this section, the C_p values are taken at the moment of maximum cavitation volume.

To evaluate the robustness and physical consistency of this approach, additional time instances corresponding to successive local maxima of cavitation volume are also examined. This assessment aims to determine whether the resulting $-C_p$ profiles follow a coherent trend or whether the observed agreement with the reference data is coincidental.

As shown in Fig. 5, the $-C_p$ distributions at multiple cavitation peaks display consistent patterns and closely match one another. This consistency supports the assertion that the $-C_p$ profile at the moment of peak cavitation is representative of the overall cavitating behavior and can thus serve as a meaningful basis for comparison with the results reported by Malekshah et al. [15].

In Fig. 5, the labels "Local Maximum 1" through "Local Maximum 5" correspond to the first through fifth cavitation volume peaks, respectively, as identified in chronological order.

As an additional verification step, a grid independence study based on the time-averaged lift and drag coefficients ($\overline{C_l}$ and $\overline{C_d}$) was performed, with the results presented in Tab. 6. The deviation between the results obtained using the 1.020 million-cell mesh and those from the finest mesh with 3.5 million cells is approximately 0.2% for $\overline{C_l}$ and 0.1% for $\overline{C_d}$, respectively. These small differences confirm that the 1.020 million-cell mesh provides sufficient accuracy for subsequent simulations.

Furthermore, as illustrated in Figs. 5 and 6, the solution demonstrates effective grid independence at the 1.020 million-cell resolution. Therefore, this mesh size is adopted for all further analyses.

The results in Tab. 6 confirm that the deviation between the 1.020 million-cell mesh and the finest mesh with 3.686 million cells is minimal—approximately 0.2% for $\overline{C_l}$ and 0.1% for $\overline{C_d}$. This indicates that the 1.020 million-cell mesh provides sufficient spatial resolution for the present study.

Furthermore, Fig. 6 demonstrates that the chosen averaging interval is adequate. Both $\overline{C_d}$ and $\overline{C_l}$ reach a quasi-steady state, exhibiting minimal temporal variation, thereby confirming that the selected averaging duration is sufficient for reliable statistical convergence.

Similar to the case without air injection, both $\overline{C_d}$ and $\overline{C_l}$ exhibit oscillatory convergence behavior. Therefore, the grid uncertainty (U_G) was estimated using the oscillatory convergence approach proposed

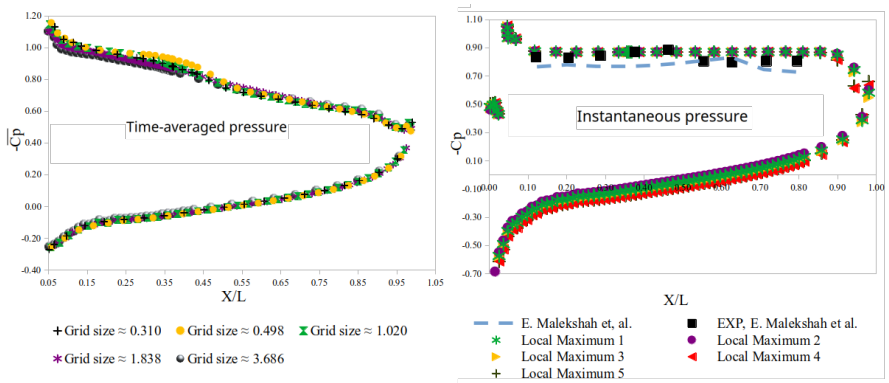

Figure 5. Left: Grid independence study of $\overline{C_p}$ along the hydrofoil surface at mid-span. Right: Comparison of instantaneous $-C_p$ values corresponding to several local maxima in cavitation volume with the experimental and numerical results of Malekshah et al. [15], considering an air injection rate of $Q = 1.0\,\mathrm{L/min}$. Grid sizes are indicated in millions of cells.

Table 6. Grid independence study based on $(\overline{C_l})$ and $(\overline{C_d})$ for an air injection rate of $Q = 1\,\mathrm{L/min}$.

Grid Size [Millions]	$(\overline{C_d})$	Rel. Change [%]	$(\overline{C_l})$	Rel. Change [%]
0.310	0.10958		0.79052	
0.498	0.10972	0.13	0.81113	2.61
1.020	0.10848	-1.14	0.79707	-1.73
1.838	0.10898	0.47	0.80269	0.71
3.686	0.10821	-0.71	0.79801	-0.58

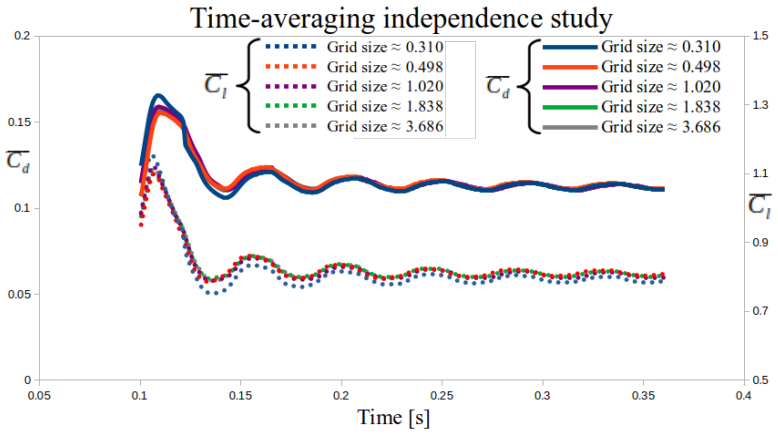

Figure 6. Time-averaging independence study based on $\overline{C_l}$ and $\overline{C_d}$ for an air injection rate of $Q = 1\,\mathrm{L/min}$.

by Stern et al. [27]. The associated uncertainty is calculated using Eqn. 13, which provides an estimate of the numerical uncertainty due to mesh resolution in cases of non-monotonic (oscillatory) convergence.

The uncertainty associated with grid refinement and the relative grid uncertainty, denoted as U_G and U_G/S_G, were computed for both $\overline{C_d}$ and $\overline{C_l}$ using the three finest mesh levels. The resulting uncertainties were 7.584×10^{-4} and 0.701% for $\overline{C_d}$, and 1.031×10^{-2} and 1.292% for $\overline{C_l}$, respectively.

As previously discussed, because the pressure coefficient C_p presented in Malekshah et al. [15] for air injection cases is based on instantaneous pressure values, a conventional uncertainty study using time-averaged pressure data is not directly applicable. Instead, in this work, a simplified comparison is performed. First, in Fig. 7, the time-averaged pressure ($\overline{p}$) at taps 1 through 11 is compared across different mesh resolutions. Subsequently, in Tab. 8, the averaged C_p values corresponding to local maxima 1–5 (as defined in Fig. 5) at taps 2 and 7 are compared with both the computational and experimental data reported by Malekshah et al. [15].

Similar to the procedure applied in the previous section, an additional mesh-sensitivity check was performed for the air-injection case using an *unsteady* metric. Specifically, the pressure signal $p(t)$ at selected taps was transformed into the frequency domain, and the spectral amplitude at the dominant shedding frequency, $A_{p'}(f_{\text{shed}})$, was extracted. The purpose of this additional check is to verify that the principal unsteady content associated with the shedding process is not abnormally sensitive to further mesh refinement.

Table 7. Grid-independence study with air injection based on the pressure-fluctuation spectral amplitude at the primary shedding frequency f_{shed}, evaluated at Tap 10 and Tap 2.

Grid size [million cells]	$A_{p'}(f_{\text{shed}})$ at Tap 10	$A_{p'}(f_{\text{shed}})$ at Tap 2
0.30	0.1375	0.0396
0.49	0.1343	0.0447
1.00	0.1322	0.0464
1.80	0.1259	0.0513
3.50	0.1246	0.0513

Based on Tab. 7, the unsteady metric $A_{p'}(f_{\text{shed}})$ exhibits reduced sensitivity as the grid is refined beyond approximately 1.0×10^6 cells. At Tap 10, the amplitude decreases from 0.13226 (1.0M) to 0.12591 (1.8M) and 0.12466 (3.5M), corresponding to changes of approximately -4.8% and -5.7% relative to the 1.0M value; notably, the difference between the two finest meshes is about -1.0%. At Tap 2, the amplitude increases from 0.04644 (1.0M) to 0.05136 (1.8M) and 0.05135 (3.5M), i.e., changes of approximately $+10.6\%$ and $+10.6\%$ relative to 1.0M, while the difference between the two finest meshes is negligible (about -0.04%). Therefore, although Tap 2 shows a larger shift between 1.0M and the finer meshes, the near-identical values for 1.8M and 3.5M indicate that the solution is essentially converged at the fine-mesh level, and the 1.0M mesh remains a practical compromise for the parametric simulations that follow.

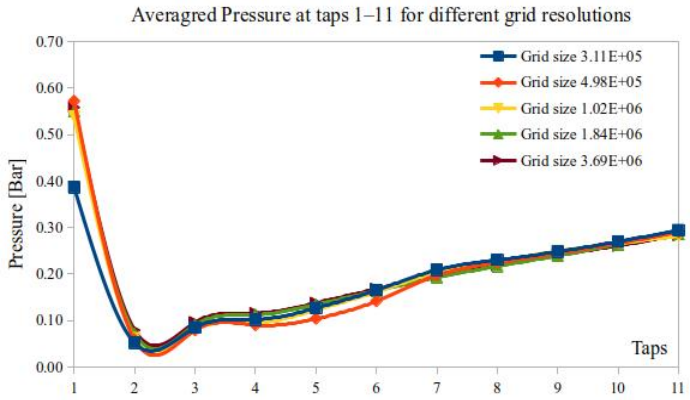

Figure 7. Averaged pressure $\overline{p}$ at taps 1 to 11 for different grid resolutions (grid sizes: 3.11×10^5, 4.98×10^5, 1.02×10^6, 1.84×10^6, and 3.69×10^6 cells).

Figure 7 summarizes the distribution of the time-averaged pressure $\overline{p}$ along the taps and its sensitivity to mesh refinement. The coarsest mesh exhibits noticeable deviations, particularly at Tap 1, whereas the intermediate and finer meshes collapse closely over the full set of taps, indicating that the predicted mean pressure levels are largely insensitive to further refinement.

Table 8. Comparison of averaged C_p values corresponding to local maxima at taps 2 and 7, with both the computational and experimental data reported by Malekshah et al. [15].

	EXP, Malekshah et al.	CFD, Malekshah et al.	Relative error	Current study	Relative error
Tap 2	0.84684	0.77110	-8.944%	0.87095	2.848%
Tap 7	0.81081	0.80129	-1.174%	0.86991	7.289%

As shown in Tab. 8, the maximum deviation of the present study from the experimental results of Malekshah et al. [15] is approximately 7.2%, which is lower than the deviation reported for Malekshah et al. CFD results.

It is noted, however, that the time-averaged pressure ($\overline{p}$) comparison across different meshes (Fig. 7) reveals local deviations of up to approximately 15% between fine mesh levels. These discrepancies are primarily attributed to the inherently unsteady nature of the three-phase flow with air injection, where localized pressure peaks are highly sensitive to transient flow structures and phase interface dynamics. Even small differences in mesh resolution can alter the instantaneous flow field sufficiently to affect the time-averaged pressure at specific tap locations.

Although the results are not in perfect agreement with the experimental measurements, the achieved accuracy, particularly when compared to the CFD predictions of Malekshah et al. [15], is considered sufficient for the purposes of the present study. The selected mesh resolution, therefore, provides a reasonable balance between computational cost and predictive capability for further investigations.

4.4. **Flow Physics**

The spanwise vorticity ω_z distributions at the mid-span plane are shown for both non-injection and injection cases in Figs. 8 and 9, respectively. In each case, four contour snapshots are presented, corresponding to successive instants at 0, one-quarter, one-half, and three-quarters of a single shedding period. These visualizations capture the creation, evolution, and shedding of vortical structures. In both cases, a Von Kármán vortex street develops downstream of the hydrofoil, indicating periodic vortex shedding associated with the cavity dynamics.

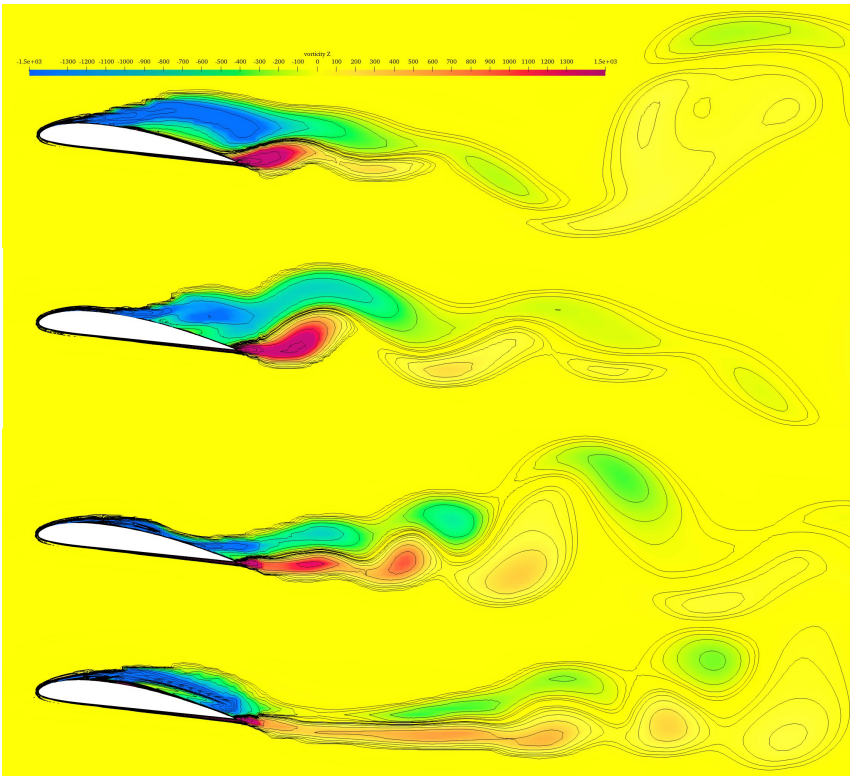

Figure 8. Spanwise vorticity ω_z on the mid-span plane for the non-injection case ($Q = 0\,\mathrm{L/min}$). Four snapshots are shown over one representative shedding cycle at phase instants $t = t_0$, $t_0 + T/4$, $t_0 + T/2$, and $t_0 + 3T/4$, where T denotes the dominant shedding period and t_0 is a reference time within the statistically stationary regime.

When air injection is applied, the vortex structures become more elongated compared to the non-injection case. This is attributed to the interaction between the injected non-condensable gas and the vapor phase, which alters the collapse dynamics and promotes a smoother transition of vortical structures. Such behavior is consistent with a cushioning effect from vapor–air merging, which is expected to reduce abrupt pressure pulses within the cavitation region.

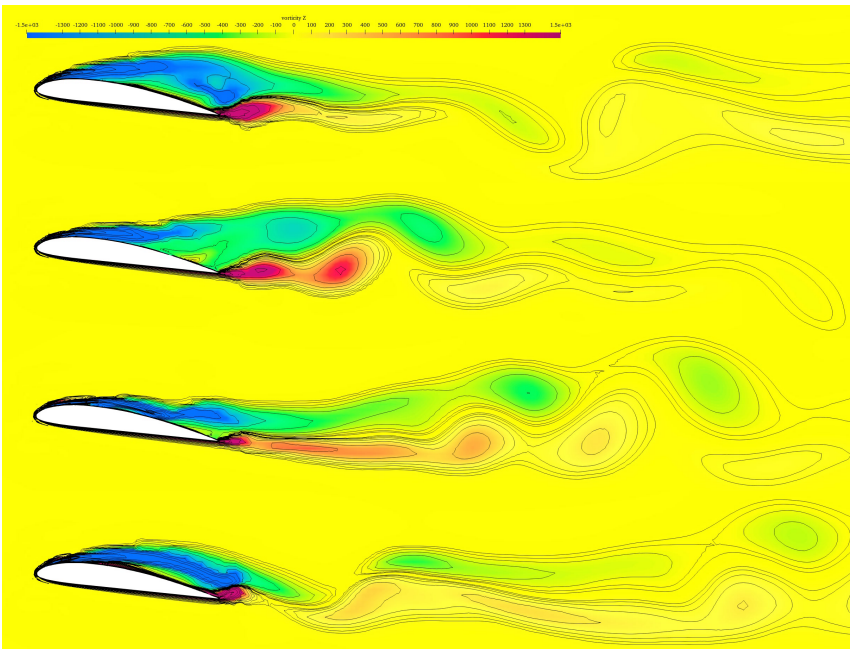

Figure 9. Spanwise vorticity ω_z on the mid-span plane for the injection case ($Q = 1\,\mathrm{L/min}$). Four snapshots are shown over one representative shedding cycle at phase instants $t = t_0$, $t_0 + T/4$, $t_0 + T/2$, and $t_0 + 3T/4$ (same definition as Fig. 8).

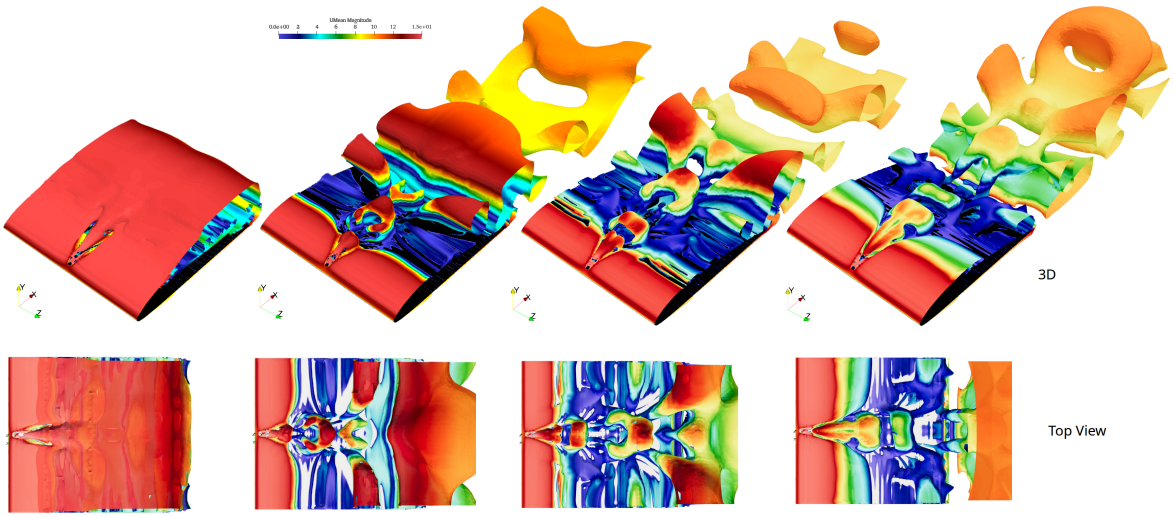

Figure 10. Q-criterion iso-surfaces over the hydrofoil with air injection ($Q = 1\,\mathrm{L/min}$).

Figure 10 presents the Q-criterion iso-surfaces visualization for the case with air injection. Similarly, four snapshots are shown, corresponding to 0, one-quarter, one-half, and three-quarters of a shedding cycle, thereby illustrating the temporal evolution of coherent vortices.

Following the description by Malekshah et al. [15], the vortex evolution over one cycle can be classified into four phases: (1) formation of the vortex structure on the suction side, (2) detachment from the hydrofoil surface, (3) primary shedding, and (4) secondary shedding. All phases are reproduced in the present simulations, confirming the solver's ability to capture observed dynamics in the literature. The influence of air injection is particularly evident during the shedding stages, where the coherence and downstream reach of the vortices are noticeably altered.

Figure 11 shows the three-dimensional Q-criterion iso-surfaces for the same case. A clear Von Kármán vortex street is visible in the wake, consistent with the spanwise vorticity (ω_z) results. In both Figs. 10 and 11, the Q-criterion iso-surfaces are colored by the mean velocity magnitude, allowing the propagation speed of individual vortex structures to be inferred. The results confirm that air injection modifies the

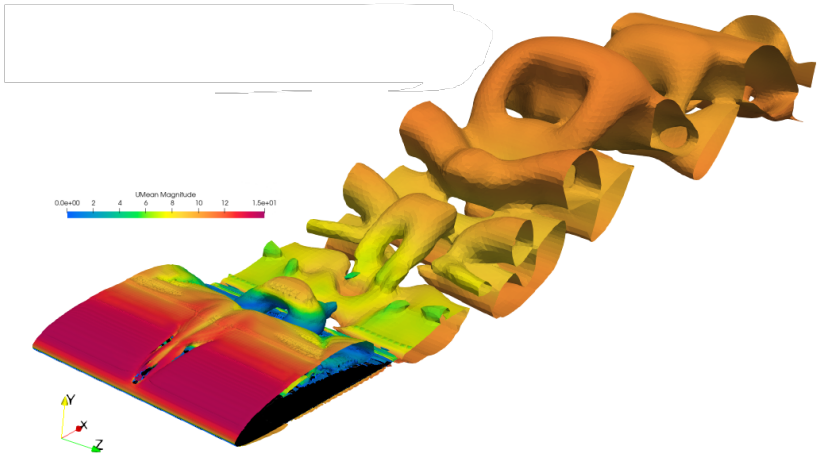

Figure 11. Three-dimensional Q-criterion iso-surfaces for the case with air injection ($Q = 1\,\mathrm{L/min}$).

spatial coherence of the wake vortices, extending their persistence downstream, in agreement with the vorticity-based observations.

4.5. **Volume Fraction Fluctuation Analysis**

To assess the effects of the merging model and air injection on the unsteady multiphase behavior, the mean square fluctuations of the volume fractions, specifically for water, vapor, and air, are shown in Figs. 12 and 13. In the case without air injection ($Q = 0\,\mathrm{L/min}$), only the water and vapor fluctuation fields are presented, since the air volume fraction remains zero throughout the domain and its fluctuation is identically zero.

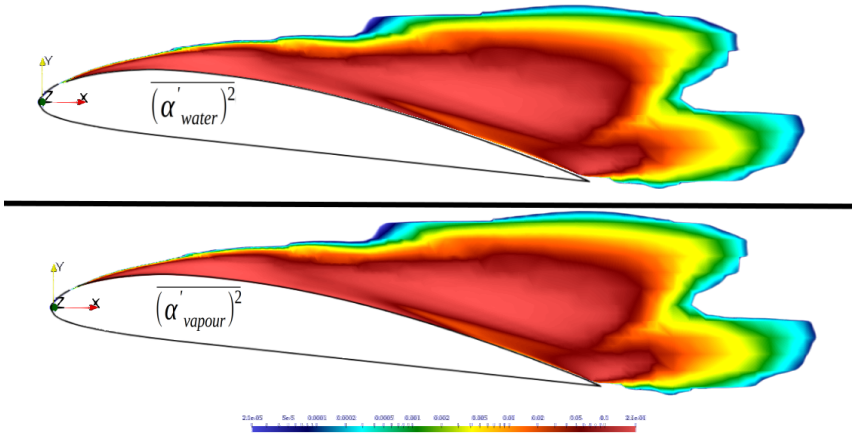

Figure 12. Mean square volume fraction fluctuations ($\overline{\alpha'^2}$) for water and vapor at mid-span, without air injection ($Q = 0\,\mathrm{L/min}$).

In contrast, the case with air injection ($Q = 1\,\mathrm{L/min}$) reveals several key features. First, the region of fluctuating water volume fraction is significantly elongated downstream, suggesting intensified mixing and turbulence due to the interaction between the injected air and the primary flow. Second, the vapor fluctuation region is not only shorter but also weaker in magnitude. This indicates that the non-condensable gas alters the collapse dynamics of vapor cavities—likely by cushioning and delaying condensation—via local pressure modification.

Additionally, the air volume fraction fluctuation field demonstrates a high concentration near the injection point, with a rapid decay downstream. This is consistent with expectations: the injected air locally disturbs the flow, generating fluctuations that dissipate gradually due to diffusion and advection.

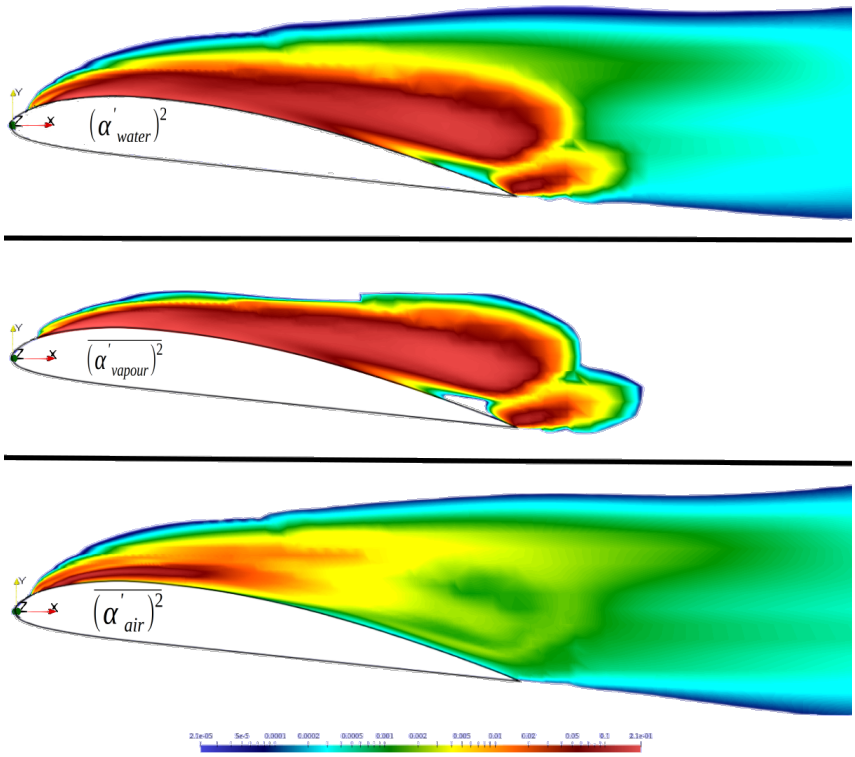

Figure 13. Mean square volume fraction fluctuations ($\overline{\alpha'^2}$) for water, vapor, and air at mid-span, with air injection ($Q = 1\,\mathrm{L/min}$).

Further inspection of Figs. 12 and 13 reveals a strong spatial correlation between vapor and air fluctuations near the cavity closure region. This overlapping behavior implies a stabilizing effect of the injected air on the vapor–liquid interface, reducing irregular cavitation cloud shedding and potentially mitigating violent collapse events.

Moreover, the smoother and more compact vapor fluctuation region in the air-injected case suggests a suppression of violent bubble dynamics. The water and air fluctuation trails both extend further into the wake, indicating enhanced three-phase interaction and transport downstream. This has implications for flow-induced noise, hydrodynamic efficiency, and erosion risk in practical applications.

4.6. **Cavitation Analysis**

As a next step, a comparison of the cavitation area at the mid-span slice of the computational domain is presented in Fig. 14 for both cases with and without air injection. In this figure, the air-injection case corresponds to injection from tap 5 (see Fig. 1).

The cavity boundary extracted from experimental flow visualization is inherently dependent on the image-processing methodology and the optical characteristics of the measurement system. In the experiments reported by Malekshah et al. [11, 15], the cavity envelope is obtained using a mean gray-level approach, in which the temporal average of the pixel intensity is used to distinguish regions containing gas (vapor and injected air) from pure liquid water. It should be emphasized that this method does not identify a sharp phase interface; rather, it delineates an optically detectable region in which a sufficient gas content modifies light transmission and scattering.

Previous experimental studies indicate that bubbly or cavitating regions become visually distinguishable once the local gas volume fraction reaches several percent, with the effective detectability depending on illumination intensity, camera resolution, bubble-size distribution, and optical path length. Liu and Hong [30] reported that cavity shapes extracted from backlit high-speed images correspond closely to regions with approximately 5–10% gas content, rather than to a liquid–gas interface in a strict volumetric sense. Similarly, Zhang et al. [31] showed that gray-level-based cavity detection is sensitive to experimental lighting conditions and bubble population, and that the detected boundary represents an optically visible bubbly mixture rather than a fully vapor-filled region.

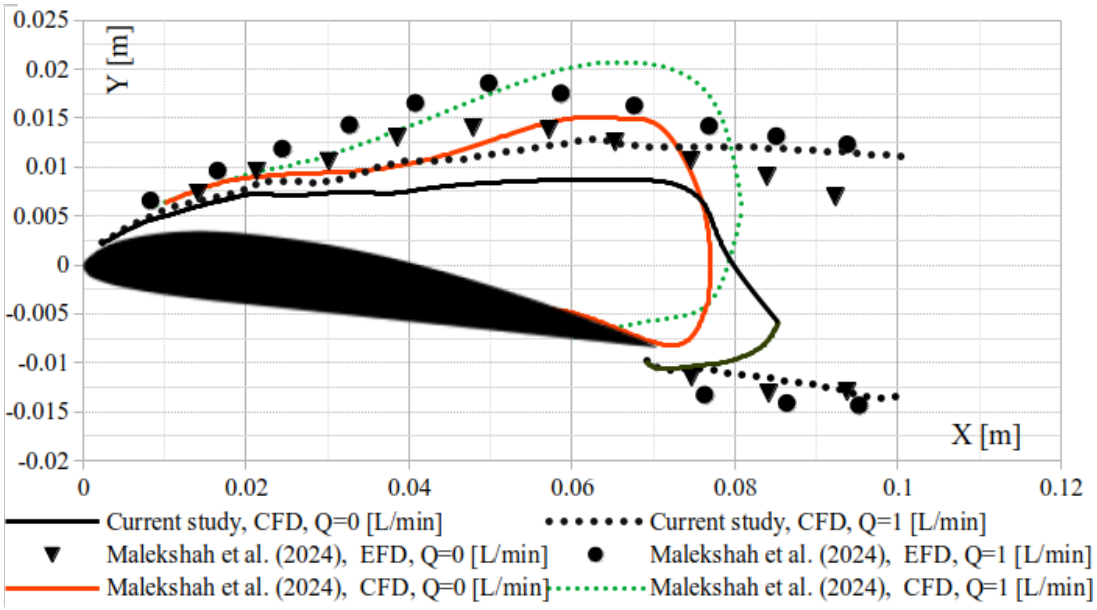

Figure 14. Comparison of time-averaged cavitation regions at the mid-span slice of the computational domain with the experimental fluid dynamics (EFD) data of Malekshah et al. [15]. The air-injection case corresponds to injection from Tap 5.

In the experimental data of Malekshah et al., the exact gray-level threshold used to delineate the cavity boundary is not explicitly specified, and the resulting envelope is manually extracted for comparative purposes. Considering the relatively strong backlighting employed in those experiments and the spatial resolution of the Phantom Miro C110 camera, it is reasonable to assume that regions with a combined gas volume fraction on the order of 5% are already optically distinguishable from pure liquid. As shown in Fig. 14, this interpretation yields cavity shapes that closely correspond to the experimentally observed envelopes and improves agreement relative to previously reported CFD cavity contours, while remaining consistent with established interpretations of gray-level-based cavitation visualization.

A further observation, also reported in the reference study, is the increase in cavitation area under air injection. This trend is reproduced in the present results and highlights the interaction between injected non-condensable gas and the vapor phase.

4.7. **Pressure Fluctuation Analysis**

To further investigate the influence of air injection and the merging model on flow unsteadiness, Fig. 15 shows the distribution of mean square pressure fluctuations, $\overline{p'}^2$, for both simulated cases. The upper panel corresponds to the scenario without air injection ($Q = 0\,\mathrm{L/min}$), while the lower panel represents the case with air injection ($Q = 1\,\mathrm{L/min}$).

In the absence of air injection, pressure fluctuations are mostly localized near the cavity closure region (close to the trailing edge), with a relatively broad but moderate magnitude. This distribution is consistent with classical cavitating flows, where periodic cloud shedding and vapor collapse generate unsteady pressure fields.

Upon activation of air injection, both the intensity and the spatial spread of $\overline{p'}^2$ increase significantly, especially in the wake region. The amplified fluctuation levels suggest a stronger interaction between the collapsing vapor and the injected non-condensable gas. This behavior aligns with observations by Hilo et al. [17], who reported increased pressure instability with gas entrainment. These interactions likely introduce localized compression and expansion events, further enhancing transient pressure peaks.

Such intensified fluctuations have important implications: they may contribute to increased flow-induced vibration, noise generation, and potential material erosion. Notably, although air injection is often used to mitigate violent cavitation collapse, it appears to simultaneously introduce new unsteady phenomena driven by three-phase dynamics.

Interestingly, while the air injection alters vapor dynamics (as shown in the volume-fraction fluctuation distributions in Figs. 12 and 13), it also introduces an additional instability source that manifests clearly in the pressure fluctuation field. This highlights a trade-off: while injected air may reduce violent cavitation

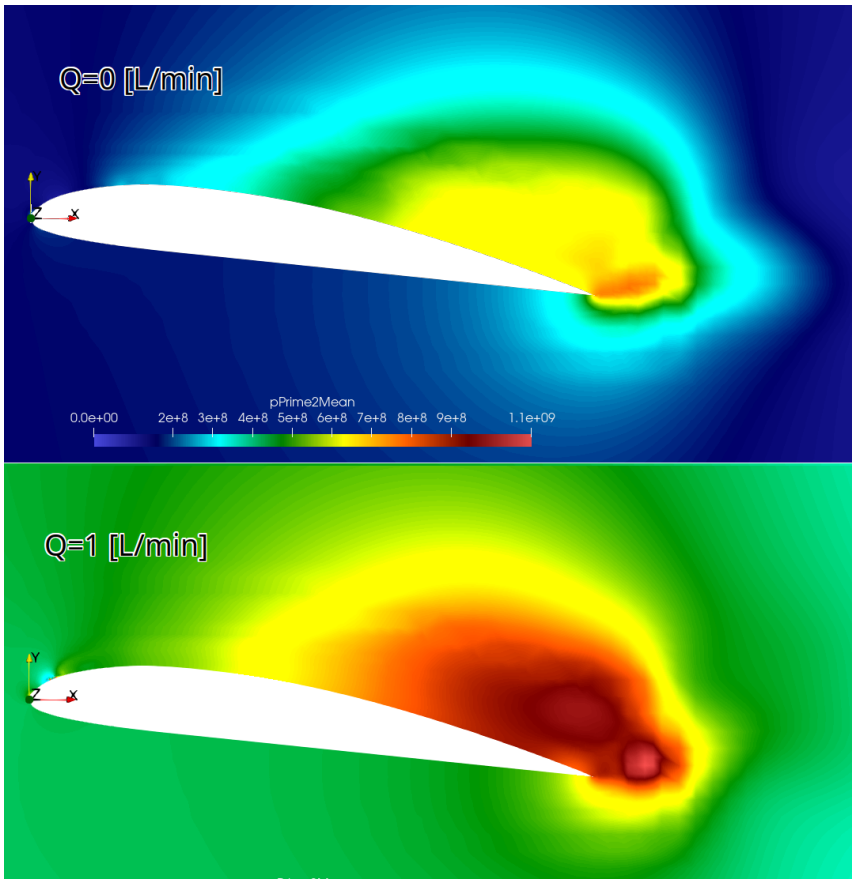

Figure 15. Mean square pressure fluctuation $\overline{p'}^2$ at mid-span for both cases: top, without air injection ($Q = 0\,\mathrm{L/min}$), bottom, with air injection ($Q = 1\,\mathrm{L/min}$).

collapse locally, it may also contribute to new unsteady features elsewhere in the flow domain. Consistent with the spectral analysis presented below, the overall enhancement of pressure fluctuations with air injection arises primarily from an increase in the high-frequency (1000 to 5000 Hz) components, rather than from a systematic rise in low-frequency energy.

The pressure frequency spectra for taps 2, 5, 8, and 11 are shown in Figs. 16 and 17 for the low–mid (10 to 1000 Hz) and high (1000 to 5000 Hz) frequency ranges, respectively. These taps are positioned from upstream of the injection location (tap 2) towards the trailing edge (tap 11), allowing the spatial development of pressure fluctuations to be evaluated.

Relative spectral energy ratio. The influence of air injection is quantified using the ratio

$$R = \frac{\displaystyle\int_{f_{\min}}^{f_{\max}} \mathrm{FFT}_{\text{with air injection}}(f)\,\mathrm{d}f}{\displaystyle\int_{f_{\min}}^{f_{\max}} \mathrm{FFT}_{\text{without air injection}}(f)\,\mathrm{d}f} \tag{14}$$

where $\mathrm{FFT}_{\text{with air injection}}(f)$ and $\mathrm{FFT}_{\text{without air injection}}(f)$ are the amplitude spectra for the injection and non-injection cases, respectively, integrated over the frequency range $[f_{\min}, f_{\max}]$. Values $R > 1$ indicate an increase in spectral energy with air injection, while $R < 1$ indicates a reduction.

Low–mid frequencies (10 to 1000 Hz). The $R_{\text{low-mid}}$ values are above unity for taps 1 to 5, indicating a slight increase in low-frequency spectral energy with air injection in the upstream and mid-chord region. From taps 6 to 9, R is approximately unity or slightly below, showing no consistent amplification or attenuation in this range. At tap 11, R returns to slightly above 1, suggesting comparable low-frequency content in the far wake for both cases.

High frequencies (1000 to 5000 Hz). For all taps, R_{high} is greater than 1, indicating that air injection increases the high-frequency spectral energy across the chord. The largest increase is observed at tap 1 ($R \approx 3.98$), close to the injection point. While the magnitude of R varies along the chord, it remains between approximately 1.7 and 4.0, showing that the increase of high-frequency content persists

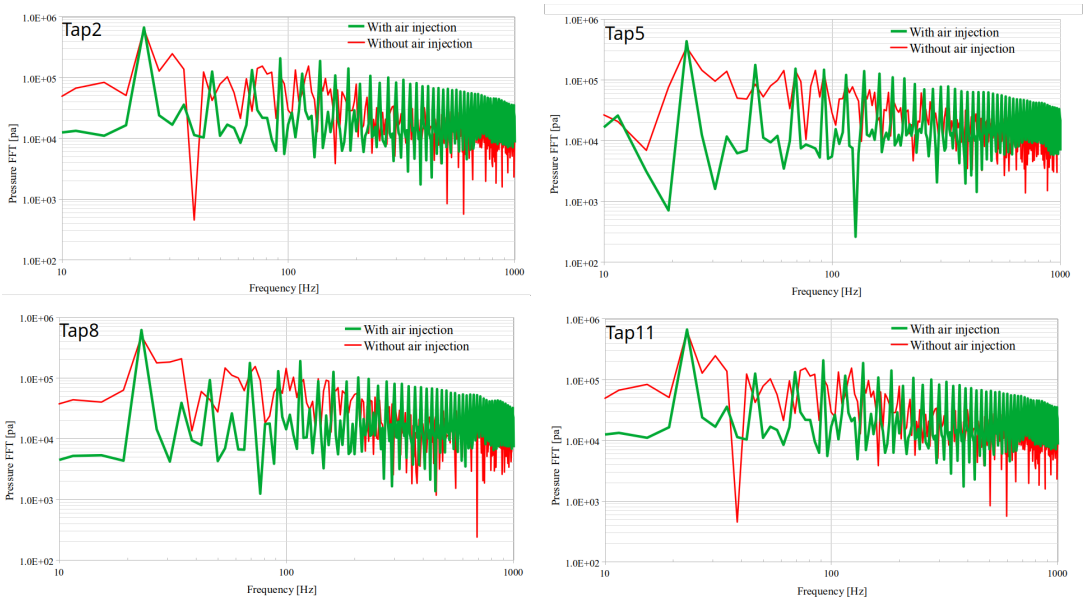

Figure 16. Pressure FFT [Pa] for the cases with and without air injection at taps 2, 5, 8, and 11; frequency range: 10 to 1000 Hz.

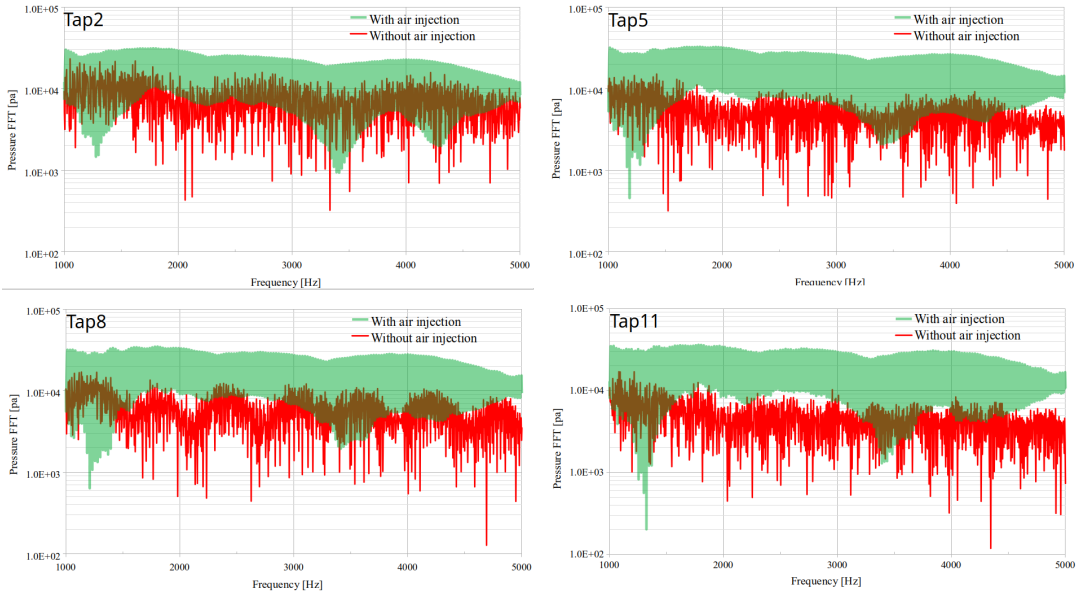

Figure 17. Pressure FFT [Pa] for the cases with and without air injection at taps 2, 5, 8, and 11; frequency range: 1000 to 5000 Hz.

downstream. Together with the near-unity (or only weakly altered) low–mid-frequency ratios in Tab. 9, this establishes that air injection enhances the overall pressure fluctuations chiefly by amplifying the high-frequency spectral content.

These results demonstrate that the main robust effect of air injection is a consistent amplification of high-frequency pressure fluctuations across all measured locations. Low-frequency changes are weaker and location-dependent, with modest upstream increases and negligible or slightly reduced values in the mid-chord region.

In [15], the experimentally measured primary shedding frequency for the case without air injection and with $Q = 1\,\mathrm{L/min}$ air injection was reported as approximately 11.5 Hz and 10.7 Hz, respectively. Examining the same frequency region in Fig. 16, a reduction in the corresponding FFT amplitude can be observed for the case with air injection.

Table 9. Relative change R for low–mid (10 to 1000 Hz) and high (1000 to 5000 Hz) frequency ranges at different tap locations.

Tap	$Location[mm]$	$R_{\text{low-mid}}$	R_{high}
Tap1	2.8	2.807	3.982
Tap2	8.4	1.272	1.712
Tap3	14.1	1.042	1.861
Tap4	19.8	1.013	2.545
Tap5	25.4	1.027	2.781
Tap6	31.1	0.977	2.786
Tap7	36.8	0.961	2.732
Tap8	42.4	1.001	2.492
Tap9	48.1	0.993	3.053
Tap10	53.8	1.069	3.300
Tap11	59.5	1.078	3.440

5. Conclusion

Numerical simulations of a hydrofoil with and without air injection were performed to investigate the role of non-condensable gas on unsteady cavitating flow. The results demonstrate that air injection modifies both the vortex structure and the spectral characteristics of the flow. Spanwise vorticity and Q-criterion fields show that air injection elongates the vortex structures downstream of the cavity closure, consistent with a smoother collapse process due to air–vapor mixing. In [15], the experimentally measured primary shedding frequencies for the non-injection and $Q = 1$ L/min air injection cases were approximately 11.5 Hz and 10.7 Hz, respectively. Examination of the same frequency region in the present pressure spectra confirms a reduction in the corresponding FFT amplitude for the injection case. The integrated spectral energy ratio R in the low–mid frequency range (10–1000 Hz) remains close to unity for most taps, indicating that large-scale coherent structures are only weakly influenced beyond the near-injection region. In contrast, in the high-frequency range (1000–5000 Hz), R is consistently greater than unity—reaching up to about 4.0 near the injection point—demonstrating a strong and persistent amplification of small-scale pressure fluctuations caused by vapor–air interactions and enhanced bubble fragmentation. While the high-frequency amplification persists downstream, its magnitude decreases with distance, whereas changes in low-frequency content remain localized. Overall, the findings indicate that air injection primarily impacts small-scale, high-frequency flow phenomena.

Acknowledgements

The authors acknowledge gratefully the support of the German Federal Ministry for Economic Affairs and Climate Action within the framework of the projects 03SX530E and 03SX530A monitored by Dr. J. Turnow. The authors also thank Jastram GmbH & Co. KG for providing geometric data of their bow thruster. The authors gratefully acknowledge the computing time provided on the high-performance computer HoreKa by the National High-Performance Computing Center at KIT (NHR@KIT). The authors gratefully acknowledge the computing resources provided by the high-performance computing system Haumea at the University of Rostock and express their sincere thanks to the colleagues whose support made these computations possible.

Author's Contribution

M.K. performed the computations and implemented the solver developments. N.K. supervised and coordinated the project. Both authors contributed to the data analysis and manuscript preparation. All authors reviewed, edited, and approved the final version of the manuscript.

Code and data availability

The solver implementation and the OpenFOAM case setups required to reproduce the main results of this study are publicly available on GitHub:

- https://github.com/Mehrdad-1991/inter3PhasemergingChangeFoam.

The test-case repository contains three separate runnable configurations:

- `Without-airInjection`: baseline cavitating hydrofoil case without air injection, corresponding to $Q = 0$ L/min;

- `With-airInjection_FROM_Tap1_Q1LperMin`: main air-injection case with $Q = 1$ L/min through Tap 1;
- `With-airInjection_FROM_Tap5_Q1LperMin`: additional air-injection validation case with $Q = 1$ L/min through Tap 5, used for the cavitation-area comparison in Fig. 14.

Each case folder includes the corresponding OpenFOAM dictionaries, run and cleaning scripts, and post-processing scripts required to reproduce the reported quantities.

References

[1] C. E. Brennen, *Fundamentals of Multiphase Flow*. Cambridge University Press, 2005.

[2] R. Knapp, "Recent investigations of the mechanics of cavitation and cavitation damage," *Trans. ASME*, vol. 77, pp. 1045–1054, 1955.

[3] T. Sun, Y. Wei, L. Zou, Y. Jiang, C. Xu, and Z. Zong, "Numerical investigation on the unsteady cavitation shedding dynamics over a hydrofoil in thermo-sensitive fluid," *Int. J. Multiphase Flow*, vol. 111, pp. 82–100, 2019.

[4] C. Peng, S. Tian, G. Li, and M. Sukop, "Simulation of multiple cavitation bubbles interaction with single-component multiphase lattice boltzmann method," *Int. J. Heat Mass Transf.*, vol. 137, pp. 301–317, 2019.

[5] Z. He, H. Zhou, L. Duan, M. Xu, Z. Chen, and T. Cao, "Effects of nozzle geometries and needle lift on steadier string cavitation and larger spray angle in common rail diesel injector," *Int. J. Eng. Res.*, vol. 22, pp. 2673–2688, 2021.

[6] E. H. Malekshah, W. Wróblewski, K. Bochon, and M. Majkut, "Evaluation of modified turbulent viscosity on shedding dynamic of three-phase cloud cavitation around hydrofoil - numerical/experimental analysis," *International Journal of Heat and Mass Transfer*, vol. 32, pp. 3863–3880, 2022.

[7] M. Timoshevskiy, I. Zapryagaev, K. Pervunin, L. Maltsev, D. Markovich, and K. Hanjalić, "Manipulating cavitation by a wall jet: experiments on a 2d hydrofoil," *Int. J. Multiphase Flow*, vol. 99, pp. 312–328, 2018.

[8] B. Che, L. Cao, N. Chu, D. Likhachev, and D. Wu, "Effect of obstacle position on attached cavitation control through response surface methodology," *J. Mech. Sci. Technol.*, vol. 33, pp. 4265–4279, 2019.

[9] E. Kadivar, M. Timoshevskiy, K. Pervunin, and O. el Moctar, "Cavitation control using cylindrical cavitating-bubble generators (ccgs): experiments on a benchmark cav2003 hydrofoil," *Int. J. Multiphase Flow*, vol. 125, p. 103186, 2020.

[10] A. Hilo, B. Song, M. Ali, S. Ahmad, K. Qasim, and H. Jin, "Cavitating flow control and noise suppression using air injection," *Ocean Eng.*, vol. 293, p. 118728, 2024.

[11] E. H. Malekshah, W. Wroblewski, K. Bochon, and M. Majkut, "Experimental analysis on dynamic/morphological quality of cavitation induced by different air injection rates and sites," *Phys. Fluids*, vol. 35, p. 013314, 2023.

[12] Y. Mao, J. Zhang, G. Wang, D. Wu, and B. Huang, "Experimental study on effects of air injection on cavitation pressure pulsation and vibration in a centrifugal pump with inducer," *Ocean Engineering*, vol. 295, p. 118849, 2024.

[13] H. Yoon, Y. Kim, H. Chung, and K. Kim, "Internal flows of ventilated partial cavitation," *Int. J. Multiphase Flow*, vol. 126, p. 103246, 2020.

[14] A. Yu, Z. Qian, J. Ji, Q. Tang, H. Chen, and D. Zhou, "Numerical simulation of ventilated cavitation evolution with an insight on how ventilation influences pressure fluctuation and cavitation noise," *J. Appl. Fluid Mech.*, vol. 13, pp. 1727–1741, 2020.

[15] E. H. Malekshah, W. Wroblewski, and M. Majkut, "Investigation on natural to ventilated cavitation considering the air-vapor interactions by merging theory with insight on air jet location/rate effect," *International Journal of Heat and Mass Transfer*, vol. 220, p. 124968, 2024.

[16] L. Hao, J. Yang, Z. Wang, Q. Zhang, and H. Su, "Experimental investigation on the ventilated cavitating flow characteristics around an axisymmetric body with an unsteady ventilation," *Ocean Engineering*, vol. 289, p. 118222, 2024.

[17] A. K. Hilo, Y.-J. Kim, J.-W. Hong, and B.-K. Ahn, "An experimental study on the effect of air injection around the leading edge of a three-dimensional hydrofoil for cavitation noise reduction," *Ocean Engineering*, vol. 333, p. 121430, 2025.

[18] H. G. Weller, G. Tabor, H. Jasak, and C. Fureby, "A tensorial approach to computational continuum mechanics using object orientated techniques," *Computers in Physics*, vol. 12, pp. 620–631, 1998.

[19] W. Yuan and G. Schnerr, "Numerical simulation of two-phase flow in injection nozzles: Interaction of cavitation and external jet formation," *J. Fluids Eng.*, vol. 125, pp. 963–969, 2003.

[20] F. Giussani, F. Piscaglia, G. Saez-Mischlich, and J. Helie, "A three-phase vof solver for the simulation of in-nozzle cavitation effects on liquid atomization," *J. Comput. Phys.*, vol. 406, p. 109068, 2020.

[21] B. C. Dueholm, J. d. C. Christiansen, B. Endelt, N. Kristensen, and J. Hærvig, "Implementation of a VoF solver with phase change for the simulation of internal cavitation and droplet breakup in injectors," *OpenFOAM® Journal*, vol. 4, pp. 62–78, 2024.

[22] H. Cheng, X. Long, B. Ji, X. Peng, and M. Farhat, "A new euler-lagrangian cavitation model for tip-vortex cavitation with the effect of non-condensable gas," *Int. J. Multiphase Flow*, vol. 134, p. 103441, 2021.

[23] E. H. Malekshah and W. Wróblewski, "Merging theory-based cavitation model adaptable with non-condensable gas effects in prediction of compressible three-phase cavitating flow," *Int. J. Heat Mass Transf.*, vol. 196, p. 123279, 2022.

[24] E. Vasilakis, N. Kyriazis, P. Koukouvinis, M. Farhat, and M. Gavaises, "Cavitation induction by projectile impacting on a water jet," *Int. J. Multiphase Flow*, vol. 114, pp. 128–139, 2019.

[25] F. R. Menter, "Two-equation eddy-viscosity turbulence models for engineering applications," *AIAA Journal*, vol. 32, no. 8, pp. 1598–1605, 1994.

[26] H. Jasak, "Error analysis and estimation for the finite volume method with applications to fluid flows," Ph.D. thesis, Imperial College of Science, Technology and Medicine, London, UK, 1996.

[27] F. Stern, R. V. Wilson, H. W. Coleman, and E. G. Paterson, "Verification and validation of cfd simulations," 1999.

[28] M. Kazemi, N. Kornev, and J. Hinnenthal, "Scale resolving simulation of unsteady bow thruster hydrodynamics," *Ocean Engineering*, vol. 298, p. 117212, 2024.

[29] S.-H. Heo and Y.-J. Kim, "Periodic behavior and noise characteristics of cavitating flow around two-dimensional hydrofoils," *Journal of Marine Science and Engineering*, vol. 12, no. 9, p. 1681, 2024. [Online]. Available: https://www.mdpi.com/2077-1312/12/9/1681

[30] D. Liu and F. Hong, "Numerical prediction of smp'11 propeller performance with and without cavitation," in *Proceedings of the Second International Symposium on Marine Propulsors (SMP'11)*, Hamburg, Germany, 2011.

[31] X. Zhang, J. Wang, M. Xu, Q. Lyu, and B. Ji, "Experimental study of pressure and velocity fluctuations induced by cavitation in a small venturi channel," *Energies*, vol. 13, no. 24, p. 6478, 2020.

Appendix A. Governing equations for a three-phase VOF formulation with phase change and merging-pressure closure

This appendix states the governing equations in the notation consistent with the `interFoam` family solvers and summarizes the three-phase Schnerr-Sauer cavitation formulation and the merging-pressure closure as implemented in the present OpenFOAM solver. The system consists of three immiscible phases: liquid (1), vapor of the liquid (2), and a non-condensable gas (3). A one-field (mixture) velocity $\mathbf{U}$ is solved for all phases.

A.1. Model assumptions and primary unknowns

We introduce the phase volume fractions $\alpha_1, \alpha_2, and\ \alpha_3$ subject to Eqn. (1), and a single velocity field $\mathbf{U}$. Each phase density ρ_i is treated as constant (incompressible, isothermal phases). The solver advects two independent fractions (α_1 and α_3) and reconstructs the third one:

$$\alpha_2 \;=\; \mathrm{clamp}(1-\alpha_1-\alpha_3,\,0,\,1)\,, \qquad \mathrm{clamp}(z,0,1)=\min(\max(z,0),1). \tag{15}$$

For numerical robustness, bounded fractions are used repeatedly:

$$\alpha_i^{*}=\min\big(\max(\alpha_i,0),1\big), \qquad i\in\{1,2,3\}. \tag{16}$$

A.2. Mixture density and transport properties

The mixture density is computed as the phase-weighted sum (see Eqn. (2)), with α_2 given by Eqn. (15). Effective viscosity (laminar+turbulent) follows the standard incompressible RANS closure used in OpenFOAM and is not repeated here.

A.3. Mixture continuity and one-field momentum equation

The mixture is advanced with a pressure velocity coupling (PIMPLE). In a one-field incompressible VOF framework with variable $\rho(\alpha_i)$, the governing equations may be written in conservative form as

$$\frac{\partial \rho}{\partial t}+\nabla\cdot(\rho\mathbf{U})=0, \tag{17}$$

$$\frac{\partial(\rho\mathbf{U})}{\partial t}+\nabla\cdot(\rho\mathbf{U}\otimes\mathbf{U})=-\nabla p+\nabla\cdot\boldsymbol{\tau}_{\mathrm{eff}}+\rho\mathbf{g}+\mathbf{f}_\sigma, \tag{18}$$

where $\boldsymbol{\tau}_{\mathrm{eff}}$ denotes the effective viscous/turbulent stress tensor and $\mathbf{f}_\sigma$ is the surface-tension force.

A.4. Surface tension and curvature (VOF continuum surface force)

The solver employs a continuum surface-force formulation. The curvature is obtained from an interface-normal flux based on $\nabla\alpha_1$ (see `threePhaseInterfaceProperties`):

$$\mathbf{n}=\frac{\nabla\alpha_1}{\|\nabla\alpha_1\|+\delta_N}, \tag{19}$$

$$K=-\nabla\cdot\mathbf{n}, \tag{20}$$

with a small regularization $\delta_N>0$. The corresponding force is

$$\mathbf{f}_\sigma \;=\; \sigma K\nabla\alpha_1, \tag{21}$$

with σ the (effective) surface-tension coefficient used by the solver.

A.5. **Pressure formulation using p_{rgh}**

As in `interFoam`, the solver uses the hydrostatic split

$$p_{rgh} \;=\; p - \rho\,\mathbf{g}\cdot\mathbf{x}, \tag{22}$$

and solves for p_{rgh} inside the PIMPLE corrector loop. The pressure equation is assembled such that Eqn. (17) is satisfied after each correction; the detailed discrete form follows the standard OpenFOAM derivation for variable-density incompressible VOF solvers and is omitted for brevity.

A.6. **VOF transport equations with compressive flux**

The VOF advection employs an additional compressive flux to maintain sharp interfaces. In OpenFOAM notation, the generic form used by MULES-type updates is

$$\frac{\partial \alpha}{\partial t} + \nabla\cdot(\alpha\mathbf{U}) + \nabla\cdot(\alpha(1-\alpha)\mathbf{U}_c) - \alpha\,\nabla\cdot\mathbf{U} = S_\alpha, \tag{23}$$

where $\mathbf{U}_c$ is the artificial compression velocity (controlled by `cAlpha` in the solver dictionaries), and the term $-\alpha\nabla\cdot\mathbf{U}$ is retained ("compression term").

In the present three-phase implementation, two transport equations are solved:

$$\frac{\partial \alpha_1}{\partial t} + \nabla\cdot(\alpha_1\mathbf{U}) + \nabla\cdot(\alpha_1(1-\alpha_1)\mathbf{U}_{c,1}) - \alpha_1\,\nabla\cdot\mathbf{U} = S_{\alpha_1}, \tag{24}$$

$$\frac{\partial \alpha_3}{\partial t} + \nabla\cdot(\alpha_3\mathbf{U}) + \nabla\cdot(\alpha_3(1-\alpha_3)\mathbf{U}_{c,3}) - \alpha_3\,\nabla\cdot\mathbf{U} = 0, \tag{25}$$

and α_2 is reconstructed by Eqn. (15). The gas phase is non-condensing and non-reacting in the present phase-change model; it enters only through boundary conditions and through the merging-pressure closure described later.

A.7. **Phase-change coupling terms in OpenFOAM form**

Phase change is modeled as interphase mass transfer between phases $1 \leftrightarrow 2$. In the solver, the phase-change model provides two paired source terms that are used (i) in the α_1 equation and (ii) in the pressure equation.

The phase-change base class returns `mDotAlphal()` and `mDotP()` as pairs:

$$\mathrm{Pair}\big(m^{(0)}, m^{(1)}\big),$$

which represent the two contributions (condensation-like and vaporisation-like parts) assembled with sign-controlled operators.

The source used in the α_1 transport is provided as `vDotAlphal()`:

$$\left(v\dot{\alpha}_1\right)^{(k)} = \alpha_{\ell,\mathrm{coeff}}\, m^{(k)}_{\alpha_\ell}, \qquad k \in \{0,1\}, \tag{26}$$

with the coefficient exactly as implemented in `phaseChangeThreePhaseMixture`:

$$\alpha_{\ell,\mathrm{coeff}} = -\frac{1}{\rho_1} + \alpha_1\left(\frac{1}{\rho_1} - \frac{1}{\rho_2}\right). \tag{27}$$

Similarly, the contribution used in the p_{rgh} equation is returned as `vDotP()`:

$$\left(v\dot{p}\right)^{(k)} = p_{\mathrm{coeff}}\, m^{(k)}_{p}, \qquad p_{\mathrm{coeff}} = \left(\frac{1}{\rho_2} - \frac{1}{\rho_1}\right), \tag{28}$$

where `mDotP()` is provided by the cavitation model (Section A.8).

A.8. **Three-phase Schnerr-Sauer cavitation model with merging-pressure closure**

Cavitation is represented by transfer between liquid (1) and vapor (2). The present model follows the Schnerr-Sauer structure, with coefficients C_c and C_v, nuclei number density n, and nuclei diameter d_{Nuc}. The saturation pressure is $p_v \equiv p_{\mathrm{sat}}$ (stored as `pSat`). The non-condensable gas (3) does not exchange mass, but it modifies the effective reference pressure through a merging-pressure closure, which enters all kinetics through p_m.

A.8.1. *Nuclei volume fraction and bubble radius.* The nuclei "volume" quantity and the nuclei volume fraction are

$$V_{\text{nuc}} = \frac{n\pi d_{\text{Nuc}}^3}{6}, \qquad \alpha_{\text{nuc}} = \frac{V_{\text{nuc}}}{1 + V_{\text{nuc}}}. \tag{29}$$

The bubble radius used by the model is a function of the bounded liquid fraction α_1^*:

$$R_b(\alpha_1^*) = \left[\frac{3}{4\pi n} \max\left(\frac{1 + \alpha_{\text{nuc}} - \alpha_1^*}{\max(\alpha_1^*, 10^{-3})},\ \text{ROOTVSMALL} \right) \right]^{1/3}. \tag{30}$$

This expression matches `Rb()` in the code, including the cutoff $\max(\alpha_1^*, 10^{-3})$.

A.8.2. *Merging-pressure closure (implemented form).* The implementation-level form of the merging-pressure closure introduced in Section 2 is repeated here for completeness, because the source-term expressions below depend explicitly on p_m. The merging closure is computed from bounded α_2^*, α_3^* and a fixed $\gamma = 1.4$. First define

$$p_{g2} = \max(p - p_v, 0), \qquad r = \max\left(\frac{\alpha_3^*}{\alpha_2^* + \varepsilon}, \varepsilon \right), \tag{31}$$

with $\varepsilon = \texttt{SMALL} > 0$. The merged pressure is

$$p_{m,\text{merged}} = p_v + p_{g2}\, r^\gamma. \tag{32}$$

The activation coefficient $M \in \{0, 1\}$ is built from two conditions implemented via `pos` and `min`:

$$M = \min(H(0.99 - \alpha_1^*),\ H(\alpha_2^* - \alpha_3^*)), \tag{33}$$

where $H(\cdot)$ is the Heaviside step (OpenFOAM `pos`). The effective reference pressure used in cavitation kinetics is then

$$p_m = M\, p_{m,\text{merged}} + (1 - M)\, p_v. \tag{34}$$

Eqns. (32) and (34) reproduce exactly the logic implemented in `pCoeff()`, `mDotAlphal()`, and `mDotP()`.

A.8.3. *Auxiliary mixture-density factors used in the implementation.* The code constructs (i) a bounded mixture density and (ii) an additional density ratio used in the source terms. With bounded fractions,

$$\rho^* = \max(\alpha_1^* \rho_1 + \alpha_2^* \rho_2 + \alpha_3^* \rho_3,\ \rho_2), \tag{35}$$

and

$$\chi = \frac{\rho^* + \alpha_3^*(\rho_2 - \rho_3)}{\rho^* + \alpha_3^*(\rho_1 - \rho_3)}. \tag{36}$$

These match `rho` and `densityfrac` in the code.

A.8.4. *Kinetic prefactor (`pCoeff` function).* The kinetic prefactor returned by `pCoeff(p)` is

$$\Pi(p) = \left(\frac{\rho_1 \rho_2}{\rho^* + \alpha_3^*(\rho_1 - \rho_3)} \right) \sqrt{\frac{2}{3\rho_1}} \sqrt{\frac{1}{|p - p_m| + 0.01\, p_m}}, \tag{37}$$

where p_m is given by Eqn. (34). This is the exact algebra appearing in the return expression of `pCoeff()`.

A.8.5. *Mass-transfer source terms for α_1: `mDotAlphal`.* The solver defines $p_0 = 0$ (stored as `p0_`) and uses $\max(\cdot, p_0)$ and $\min(\cdot, p_0)$ to select the sign of the driving pressure difference. With $R_b = R_b(\alpha_1^*)$, $\Pi = \Pi(p)$, and χ as above, the pair returned by `mDotAlphal()` is

$$m_{\alpha_\ell}^{(0)} = (-C_c)\, \frac{3\,\Pi\, \max(p - p_m, p_0)}{R_b + R_b^4 \left(\frac{4}{3}\pi n\right) \chi}, \tag{38}$$

$$m_{\alpha_\ell}^{(1)} = (-C_v)\, \frac{4\pi n\, R_b^2\, \Pi\, \min(p - p_m, p_0)}{1 + R_b^3 \left(\frac{4}{3}\pi n\right) \chi}. \tag{39}$$

These are the exact expressions in `mDotAlphal()` (including the $-C_c$ and $-C_v$ prefactors and the denominators).

The corresponding volumetric source terms used in the α_1 equation are then obtained through Eqns. (26) and (27).

A.8.6. *Mass-transfer source terms for pressure:* `mDotP`. In `mDotP()`, the bounded combined fraction

$$\alpha_{13}^{*} = \min\big(\max(\alpha_1^{*} + \alpha_3^{*}, 0), 1\big) \tag{40}$$

is used to reduce condensation in regions occupied by liquid+gas. The returned pair is

$$m_p^{(0)} = (-C_c)\,(1 - \alpha_{13}^{*}) \left[\frac{3}{R_b + R_b^4\left(\frac{4}{3}\pi n\right)\chi}\right] H(p - p_m)\,\Pi, \tag{41}$$

$$m_p^{(1)} = (C_v)\,(\alpha_1^{*}) \left[\frac{4\pi n\, R_b^2}{1 + R_b^3\left(\frac{4}{3}\pi n\right)\chi}\right] \mathrm{neg}(p - p_m)\,\Pi, \tag{42}$$

where $H(\cdot)$ corresponds to `pos0` and $\mathrm{neg}(\cdot)$ corresponds to OpenFOAM's `neg`. These expressions reproduce the code in `mDotP()` (including the sign conventions and activation operators).

The pressure-equation volumetric source terms are then constructed as in Eqn. (28).

A.9. **Remark on reconstruction and boundedness**

The solver advances α_1 and α_3 with MULES-type bounded advection and then reconstructs α_2 using Eqn. (15). This strategy enforces the algebraic constraint in Eqn. (1) in a robust manner while maintaining $\alpha_i \in [0, 1]$ up to discretization tolerances. The cavitation model affects the flow through (i) the volumetric fraction source terms in the α_1 equation via Eqn. (26) and (ii) consistent pressure-equation sources via Eqn. (28), with the effective cavitation reference pressure p_m defined by the merging-pressure closure in Eqn. (34).